Chemical Science

REVIEW

View Article Online
View Journal | View Issue

Cite this: *Chem. Sci.*, 2024, **15**, 2323

Molecular modulation strategies for two-dimensional transition metal dichalcogenide-based high-performance electrodes for metal-ion batteries

Mingyuan Gu,[a] Apparao M. Rao,[b] Jiang Zhou[c] and Bingan Lu*[a]

Received 30th October 2023
Accepted 2nd January 2024

DOI: 10.1039/d3sc05768b

rsc.li/chemical-science

In the past few decades, great efforts have been made to develop advanced transition metal dichalcogenide (TMD) materials as metal-ion battery electrodes. However, due to existing conversion reactions, they still suffer from structural aggregation and restacking, unsatisfactory cycling reversibility, and limited ion storage dynamics during electrochemical cycling. To address these issues, extensive research has focused on molecular modulation strategies to optimize the physical and chemical properties of TMDs, including phase engineering, defect engineering, interlayer spacing expansion, heteroatom doping, alloy engineering, and bond modulation. A timely summary of these strategies can help deepen the understanding of their basic mechanisms and serve as a reference for future research. This review provides a comprehensive summary of recent advances in molecular modulation strategies for TMDs. A series of challenges and opportunities in the research field are also outlined. The basic mechanisms of different modulation strategies and their specific influences on the electrochemical performance of TMDs are highlighted.

1. Introduction

The enormous energy demand in modern society is causing excessive consumption of non-renewable energy sources and serious environment pollution. Energy resources, such as wind and solar energy, are clean and renewable, which are highly desirable for the long-term sustainable development of modern society. The main problem associated with these renewable clean energy sources is their intermittent characteristics, making energy storage systems (ESSs) necessary to store such intermittent energy for later use as a continuous and stable power. Due to their inherent advantages of low cost, long life-span, and high efficiency, secondary batteries are one of the ideal candidates for storing energy.[1] After decades of development, lithium-ion batteries (LIBs) have been successfully

Mingyuan Gu

Mingyuan Gu received his bachelor's degree in electronic science and technology from Hunan University in 2012. His research interests include the design and preparation of advanced electrolytes and electrode materials for potassium ion batteries.

Bingan Lu

Bingan Lu, professor of Hunan University, obtained his PhD in physics from Lanzhou University in 2012. He has extensive experience in aqueous electrolyte batteries, potassium ion batteries and zinc ion batteries. He has published over 250 papers in many prestigious journals, including Nature, National Science Review, Nature Sustainability, and Nature Communications, with an H-index of 83 and other-citation of ~20 000. He also is a Clarivate Highly Cited Researcher.

---

[a] School of Physics and Electronics, Hunan University, Changsha, P. R. China. E-mail: luba2012@hnu.edu.cn
[b] Department of Physics and Astronomy, Clemson Nanomaterials Institute, Clemson University, Clemson, SC 29634, USA
[c] School of Materials Science and Engineering, Central South University, Changsha, 410083, P. R. China

commercialized and are ubiquitous in our daily lives. However, the low abundance of lithium resources may restrict large-scale LIB-based ESSs.[2,3] Therefore, alternate secondary metal-ion batteries with higher earth-abundance of the corresponding metals, such as sodium ion batteries (NIBs),[4–6] potassium ion batteries (PIBs),[7–10] and zinc ion batteries (ZIBs),[11–13] have been extensively studied. Among various battery systems, electrode materials play an important role in the battery's electrochemical performance. Therefore, developing advanced electrode materials is desired for low cost, long lifespan, high efficiency, and large scale secondary electrochemical ESSs.

Normally with a formula of MX_2 (M is composed of transition metals in group 4 to group 7, and X = S, Se, Te), 2D transition metal dichalcogenides (TMDs) have attracted much attention in the field of energy storage due to their 2D structure and tunable physical and chemical properties.[14–16] In monolayer MX_2, X atoms are distributed in the outer layers, while the M atoms that form covalent bonds with X atoms are sandwiched between the two outer layers of X atoms. The adjacent MX_2 layers in TMDs are coupled by weak van der Waals (vdW) forces, and the interlayers allow the intercalation of metal ions. For example, Whittingham demonstrated that Li^+ can be inserted and extracted reversibly in the interlayer of TiS_2 at a high speed in his pioneering work.[17] In addition, the large interlayer spacing of MoS_2 (0.62 nm) theoretically makes it easy to accommodate metal ions, such as alkali metal ions (Li^+, Na^+, and K^+), Zn^{2+}, *etc.*[18–20] Furthermore, the conversion reaction of some TMDs in the deep discharge state provides them with a high theoretical specific capacity. However, structural aggregation, restacking, and limited cycling stability originating from the conversion reaction during cycling still exist.[21,22] These negative factors cause TMD electrode materials to exhibit unsatisfactory electrochemical performance in metal ion batteries.

To address these issues, a large amount of research has been conducted to tune and optimize the properties of TMDs. Different morphologies of TMDs,[23–25] such as nanoflowers,[26] nanorods,[27] *etc.*, were explored to increase the specific surface area and relieve the structural stress during cycling. The TMDs' larger specific surface area can increase the contact area with the electrolytes, which is beneficial for faster ion diffusion and better rate performance. The lower structural stress is beneficial for maintaining structural integrity and improving long-term cycling stability. Coupling with carbon materials is also one of the commonly used strategies, which can not only reduce the charge transfer impendence, but also alleviate the structural aggregation caused by vdW interaction.[28–30] The above strategies effectively enhance TMDs' electrochemical performance, but they all modify TMDs from an 'external' perspective, and the basic properties of TMDs remain unchanged. In contrast, molecular modulation strategies modify the TMD molecules from an 'internal' perspective. Molecular modulation is mainly carried out at the molecular or atomic level, through the purposeful modulation of specific parts or regions of TMD molecules, so as to realize the effective modulation of TMDs' properties. Table 1 summarizes the cycling performance of some TMDs before and after molecular modulation, showing the advantages of molecular modulation.[31–58] As a result, molecular modulation strategies are of great significance for the development of TMDs.

In this review, we will introduce and summarize various molecular modulation strategies for TMD electrodes used in metal ion batteries, including phase engineering, defect engineering, interlayer spacing expansion, heteroatom doping, alloy engineering, and bond modulation. We begin by introducing the basic properties of different TMDs. Next, we focus on the mechanisms of different modulation methods and their specific influences on the TMDs' properties for metal-ion storage. Lastly, the challenges and perspectives of TMDs as metal-ion battery electrodes are outlined. We expect that this review will help improve the overall understanding of various molecular modulation mechanisms for TMDs in the application of electrochemical storage and serve as an excellent reference for the future development of TMD-based electrodes.

2. Basic properties of TMDs

2.1 Crystal structure

Due to the different coordination and stacking sequences of transition metals, TMDs exhibit polymorphs and stacking polytypes. For monolayer TMDs, two typical coordination structures exist for metal atoms: trigonal prismatic and octahedral coordination.[59] As shown in Fig. 1a, the trigonal prismatic coordination can be expanded to hexagonal symmetry (belongs to the O_h (or D_{3h}) point group) with Bernal stacking (AbA) (the upper and lower case letters represent chalcogen and metal atoms, respectively) in the monolayer, namely, the 1H phase.[60] The octahedral coordination can be expanded to tetragonal symmetry (belongs to the D_{3d} point group) with rhombohedral stacking (AbC), namely, the 1T phase (Fig. 1b). Due to distortions, other phases can also be found, such as the 1T′ phase (Fig. 1c). As shown in Fig. 1d–f, for bulk TMDs, the three most common polymorphs are 1T, 2H, and 3R, where the letters represent trigonal, hexagonal, and rhombohedral symmetry, and the digits indicate the number of MX_2 units in the unit cell (in other words, the number of MX_2 layers in the stacking sequences).[61,62] Among them, 2H and 3R phases can both be formed by stacking the 1H phase in different ways with a stacking sequence of AbA BaB and AbA BcB CaC, respectively.[63] A single TMD can also exist in the form of various polymorphs or stacking polytypes, depending on its synthesis method. For example, natural MoS_2 usually exhibits the 2H phase. However, 1T or 3R phases are often found in synthesized MoS_2.[64,65] Among the above several phases, 1T and 2H have been widely studied in metal ion batteries.

2.2 Electronic structure

The electrical properties of TMDs depend on the transition metals' coordination environment and their d orbital filling states.[62] In both 1H and 1T phases, the non-bonding d bands of TMDs are located within the gap between the bonding and antibonding bands of M–X bonds. Due to the influence of the lattice field, the d orbitals of transition metals with trigonal prismatic coordination (O_h) split into three groups, $d_{z^2}(a_1)$,

Table 1 Summary of TMDs' cycling performance before and after molecular modulation

Materials	Cycling performance	Current density	Systems	Ref.
Phase engineering				
2H-MoS_2	16.4 mA h g^{-1} after 300 cycles	1 A g^{-1}	LIBs	31
2H-MoS_2/C	350 mA h g^{-1} after 300 cycles			
1T-MoS_2/C	870 mA h g^{-1} after 300 cycles			
2H-MoS_2@PNC	369.9 mA h g^{-1} after 250 cycles	0.5 A g^{-1}	NIBs	32
1T/2H-MoS_2@NC	389.5 mA h g^{-1} after 250 cycles			
1T/2H-MoS_2@PNC	472.6 mA h g^{-1} after 250 cycles			
MoS_2-0 T	182 mA h g^{-1} after 280 cycles	1 A g^{-1}	NIBs	33
MoS_2-9 T	310 mA h g^{-1} after 280 cycles			
2H-MoS_2	100 mA h g^{-1} after 50 cycles	0.1 A g^{-1}	NIBs	34
1T-MoS_2	410 mA h g^{-1} after 150 cycles			
2H-MoS_2NFs	308 mA h g^{-1} after 50 cycles and 63.6 mA h g^{-1} after 415 cycles	0.1 A g^{-1}, 1 A g^{-1}	NIBs	35
TiO_2–2H-MoS_2NFs	593 mA h g^{-1} after 50 cycles and 341 mA h g^{-1} after 700 cycles			
TiO–1T-MoS_2NFs	676 mA h g^{-1} after 50 cycles and 501 mA h g^{-1} after 700 cycles			
CNT@2H-MoS_2	254.6 mA h g^{-1} after 50 cycles	0.1 A g^{-1}	NIBs	36
1T-MoS_2	89.7 mA h g^{-1} after 50 cycles			
CNT@1T-MoS_2	542.3 mA h g^{-1} after 50 cycles			
2H-$MoSe_2$	~20 mA h g^{-1} after 50 cycles	0.1 A g^{-1}	ZIBs	37
1T-$MoSe_2$	138.8 mA h g^{-1} after 50 cycles			
1T-$MoSe_2$/CC	265.1 mA h g^{-1} after 50 cycles			
Defect engineering				
MoS_2	170 mA h g^{-1} after 220 cycles	0.1 A g^{-1}	LIBs	38
MoS_2/C-CPM	831 mA h g^{-1} after 220 cycles	0.2 A g^{-1}		
WS_2–SPAN-1	278 mA h g^{-1} after 450 cycles, 292 mA h g^{-1} after 1400 cycles	0.5 A g^{-1}, 2 A g^{-1}	NIBs	39
WS_2–SPAN-2	464 mA h g^{-1} after 450 cycles, 354 mA h g^{-1} after 1400 cycles			
WS_2–SPAN-3	246 mA h g^{-1} after 450 cycles and 206 mA h g^{-1} after 1400 cycles			
MoS_2	45 mA h g^{-1} after 100 cycles	0.5 A g^{-1}	NIBs	40
BD-MoS_2	354 mA h g^{-1} after 100 cycles			
NC@MoS_2	103 mA h g^{-1} after 100 cycles	0.1 A g^{-1}	NIBs	41
NC@MoS_2–Ar	430 mA h g^{-1} after 100 cycles			
NC@MoS_2–VS	495 mA h g^{-1} after 100 cycles			
VSe_2	264 mA h g^{-1} after 100 cycles and 79 mA h g^{-1} after 500 cycles	0.5 A g^{-1}, 3 A g^{-1}	PIBs	42
P–VSe_{2-x}	351 mA h g^{-1} after 100 cycles and 143 mA h g^{-1} after 1000 cycles			
Commercial WS_2	85.6 mA h g^{-1} after 50 cycles, —	0.1 A g^{-1}, 2 A g^{-1}	PIBs	43
P–WS_2	173.7 mA h g^{-1} after 50 cycles and 25.6 mA h g^{-1} after 50 cycles			
Sv–WS_2	230.8 mA h g^{-1} after 50 cycles and 93.2 mA h g^{-1} after 200 cycles			
MoS_2 750	~5 mA h g^{-1}	1 A g^{-1}	ZIBs	44
MoS_{2-x} 250	88.6 mA h g^{-1} after 1000 cycles			
VSe_2-SS	75.8 mA h g^{-1} after 1800 cycles	4 A g^{-1}	ZIBs	45
VSe_{2-x}-SS	175.8 mA h g^{-1} after 1800 cycles			
Interlayer spacing expansion				
MoS_2	248 mA h g^{-1} after 100 cycles	0.2 A g^{-1}	LIBs	46
MoS_2@PANI	701 mA h g^{-1} after 100 cycles			
MoS_2/PANI	1207 mA h g^{-1} after 100 cycles			
MoS_2	~90 mA h g^{-1} after 100 cycles	0.3 A g^{-1}	NIBs	
MoS_2@PANI	~150 mA h g^{-1} after 100 cycles			
MoS_2/PANI	456 mA h g^{-1} after 100 cycles			
c-WSe_2	61 mA h g^{-1} after 150 cycles	0.1 A g^{-1}	PIBs	47
WSNC	384 mA h g^{-1} after 200 cycles			
ns-MoS_2	~200 mA h g^{-1} after 100 cycles	0.5 A g^{-1}	PIBs	48
exp-MoS_2	~360 mA h g^{-1} after 100 cycles			
p-MoS_2	11.9 mA h g^{-1} after 1000 cycles	1 A g^{-1}	ZIBs	49
MoS_2/PANI-150	91.6 mA h g^{-1} after 1000 cycles			
Heteroatom doping				
Bulk WSe_2	69 mA h g^{-1} after 50 cycles, —	0.1 A g^{-1}, 1 A g^{-1}	NIBs	50
2H-WSe_2–2	281 mA h g^{-1} after 50 cycles and 158 mA h g^{-1} after 900 cycles			
2H-WSe_2–1	321 mA h g^{-1} after 50 cycles and 202 mA h g^{-1} after 900 cycles			
1T-WSe_2–Sn	460 mA h g^{-1} after 50 cycles and 285 mA h g^{-1} after 900 cycles			
OMSCF-500	60 mA h g^{-1} after 100 cycles and 21 mA h g^{-1} after 100 cycles	0.1 A g^{-1}, 1 A g^{-1}	NIBs	51
OMSCF-300	221 mA h g^{-1} after 100 cycles and 79 mA h g^{-1} after 100 cycles			

Table 1 *(Contd.)*

Materials	Cycling performance	Current density	Systems	Ref.
MSCF	232 mA h g^{-1} after 100 cycles and 87 mA h g^{-1} after 100 cycles			
OMSCF-400	330 mA h g^{-1} after 100 cycles and 181 mA h g^{-1} after 100 cycles			
Pristine MoS_2	~47 mA h g^{-1} after 50 cycles	1 A g^{-1}	ZIBs	52
D-MoS_2–O	281.9 mA h g^{-1} after 50 cycles			
Alloy engineering				
MoS_2	228.9 mA h g^{-1} after 400 cycles	1 A g^{-1}	LIBs	53
$Mo_{0.5}W_{0.5}S_2$	271.9 mA h g^{-1} after 400 cycles			
WS_2	205.8 mA h g^{-1} after 400 cycles			
MoS_2-NC	385.63 mA h g^{-1} after 1000 cycles	0.2 A g^{-1}	PIBs	54
$MoS_{1.5}Se_{0.5}$-NC	531.56 mA h g^{-1} after 1000 cycles			
MoS_2	18.3 mA h g^{-1} after 1000 cycles	2 A g^{-1}	PIBs	55
$MoSe_2$	114.3 mA h g^{-1} after 1000 cycles			
MoSSe	220.5 mA h g^{-1} after 1000 cycles			
MoS_2/rGO	67.6 mA h g^{-1} after 150 cycles	0.1 A g^{-1}	ZIBs	56
$MoSe_2$/rGO	44.5 mA h g^{-1} after 150 cycles			
MoSSe/rGO	210.3 mA h g^{-1} after 150 cycles			
Bond modulation				
$MoSe_2$	Almost no capacity after 20 cycles	1 A g^{-1}	LIBs	57
Red $MoSe_2$	1125.7 mA h g^{-1} after 500 cycles			
MoSe–rGO	~100 mA h g^{-1} after 60 cycles	0.1 A g^{-1}	PIBs	58
$MoSe_{2+x}$–rGO	168 mA h g^{-1} after 300 cycles			

$d_{x^2-y^2,xy}$(e), and $d_{xz,yz}$(e′), with a sizeable gap (~1 eV) between the first two groups of orbitals. The d orbitals of transition metals with octahedral coordination (D_{3d}) split into two groups, d_{z^2,x^2-y^2}(e_g) and $d_{yz,xz,xy}$(t_{2g}).[59] The filling states of non-bonding d bands play an important role in the electrical properties of TMDs. When the orbitals are fully occupied, such as in 2H-MoS_2 and 2H-$MoSe_2$,[66,67] the materials exhibit semiconducting behaviour. When the orbitals are partially filled, such as in NbS_2 and VS_2,[68,69] the materials show metallic behaviour. The phases and electrical properties of group 4–7 TMDs are summarized in Table 2.[59,61,63,70–76] In addition, although the chalcogen atoms have a smaller influence on the electronic properties of TMDs, the broadening of d bands and the corresponding decrease in bandgap with increasing chalcogen atom number can still be observed. For example, the bandgap of 2H-MoS_2, 2H-$MoSe_2$, and 2H-$MoTe_2$ decreases from 1.3 to 1.0 eV.[77]

The d electron counting of transition metals also plays a key role in selecting the preferred phase for TMDs. Group 4 TMDs with d^0 transition metal centers all possess an octahedral structure. While in group 5 TMDs (d^1), both the trigonal prismatic and octahedral structures exist. The trigonal prismatic phase accounts for the majority in group 6 TMDs (d^2), and

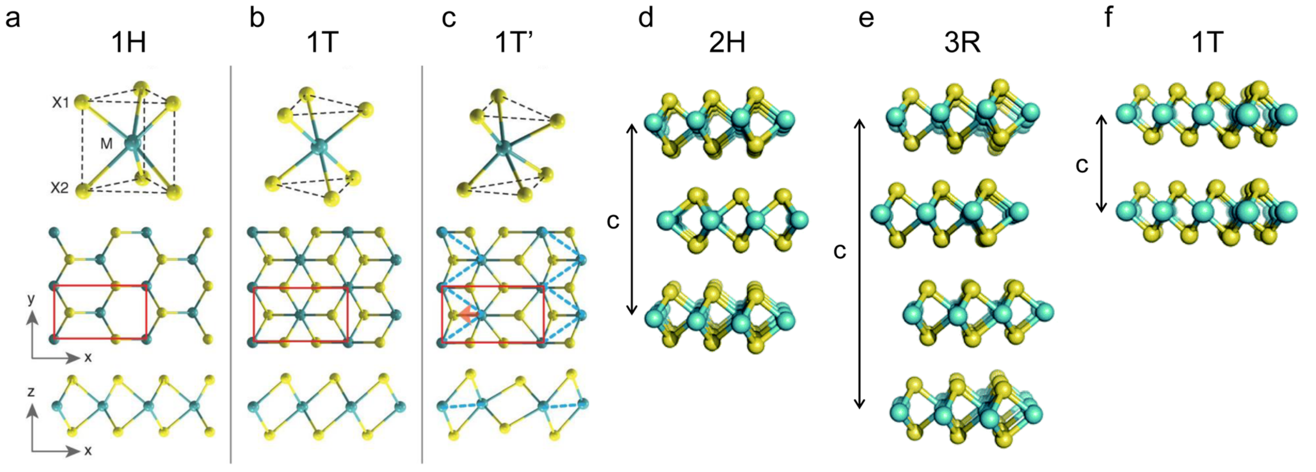

Fig. 1 Schematics of the polymorphs and stacking polytypes: (a–f) 1H, 1T, 1T′, 2H, 3R, and 1T. Reproduced with permission from (a–c) ref. 60. Copyright 2014, Science; (d–f) ref. 62. Copyright 2015, Royal Society of Chemistry.

Table 2 Summary of phases and electrical properties of TMDs

Group	Metal	Chalcogen	Phases	Electrical properties	Ref.
4	Ti	S	1T	Semiconducting	31 and 70
		Se			
		Te			
5	V	S	1T	Metal	
		Se			
		Te			71 and 72
5	Nb	S	2H	Metal	61 and 70
		Se			70 and 73
		Te	1T		61 and 70
6	Mo	S	2H	Semiconducting	61 and 70
		Se			70 and 73
		Te			61 and 70
6	W	S	2H	Semiconducting	61 and 70
		Se			70 and 73
		Te	1T′		61 and 74
7	Re	S	1T′	Semiconducting	75 and 76
		Se			61 and 63
		Te	—	—	—

group 7 TMDs (d^3) mainly consist of a distorted octahedral phase.[59]

2.3 Metal-ion storage mechanisms

When TMDs serve as alkali metal-ion battery electrodes, reversible intercalation and extraction reactions occur first at a relatively high cutoff voltage (~1 V) with A_xMX_2 as the product (A represents alkali metal atoms).[78] The M–X bonding interactions are larger than the A–MX_2 interactions during these processes. When the discharge process continues, TiX_2 and NbX_2 still exhibit reversible intercalation and extraction processes due to the sufficiently strong M–X bonding. However, for the other TMDs whose M–X bonding interactions become smaller than the A–MX_2 interactions at a low voltage, a conversion reaction occurs with the products of M and A_2X. The reversibility of the conversion reactions is influenced by the dynamic properties of MX_2,[79] including the electrical properties, structural stability, and ion diffusion kinetics. The poor dynamic properties of MX_2 result in irreversible conversion reactions and the oxidation products of M and X in the first cycle. In the subsequent cycles, the redox couple changes into X/A_2X, which means that X replaces MX_2 as the active material. Due to their poor dynamic properties, the semiconducting phases MoX_2, WX_2, and ReX_2 exhibit irreversible conversion reactions.[80–82] In contrast, the excellent dynamic properties of MX_2 lead to reversible conversion reactions, where MX_2 can be reformed after an oxidation reaction. *i.e.*, MX_2 is always the active material. The metal phase VX_2 compounds have been demonstrated to exhibit partially reversible conversion reactions due to their better dynamic properties.[83–85] In addition, the voltage at which the conversion reaction begins usually varies depending on the materials and the intercalated alkali metal ions. For example, commercial 2H-MoS_2 begins to undergo a conversion reaction when discharged to 0.6 V in a LIB system. In NIB and PIB systems, however, the starting voltages decrease to 0.13 and 0.16 V, respectively.[86]

When TMDs are used in multivalent-ion batteries, no ion storage mechanism associated with the conversion reaction has been reported so far.[87] As a result, the main multivalent-ion storage mechanisms of TMDs are currently ion intercalation and extraction.

3. Molecular modulation strategies for TMDs in metal ion batteries

3.1 Phase engineering

The pristine electrical properties of different phases play a critical role in TMDs' electrochemical performance. For example, the conversion reaction is irreversible for the semiconducting phase Mo, W, and Re-based dichalcogenides due to their poor conductivities. Due to their much better conductivity, the conversion reaction becomes partially reversible in the case of metallic phase V-based dichalcogenides. As a result, converting semiconducting phase TMDs to the metallic phase could be an effective strategy to improve their electrical properties and electrochemical performance greatly. For example, Yao *et al.* prepared 1T-MoS_2@GO for a PIB anode.[88] As a comparison, 2H-MoS_2@GO was also prepared. Due to the much improved electronic conductivity, a partially reversible conversion reaction is achieved when using 1T-phase MoS_2, which is similar to the behaviour of metallic phase V-based dichalcogenides. In addition, 1T-MoS_2@GO exhibits a better electrochemical performance than 2H-MoS_2@GO at all the tested current densities. This section mainly discusses the phase engineering strategies of Mo and W-based dichalcogenides.

As shown in Fig. 2a and b, under a trigonal prismatic crystal field, the Mo 4d orbitals of MoS_2 are divided into d_{xy,x^2-y^2}, $d_{yz,xz}$, and d_{z^2} groups, where d_{z^2} is located at the lowest position of the orbitals.[89] Therefore, the two 4d electrons fill the d_{z^2} orbital in pairs, making 2H-MoS_2 exhibit semiconducting behaviour. For 1T-MoS_2, the octahedral crystal field makes the Mo 4d orbitals split into $d_{xy,xz,yz}$ and d_{z^2,x^2-y^2} groups. In this case, the two 4d electrons tend to parallelly occupy two of the three orbitals in the lower group following the minimum Coulomb energy principle, resulting in metallic behaviour. Therefore, manipulating the electronic structures of the Mo 4d orbitals is the key to transitioning from the semiconducting phase to the metallic phase for Mo-based dichalcogenides. The partial density of states (PDOS) of Mo 4d in different phases also confirms the above conclusion (Fig. 2c and d).[89]

In addition to the greatly improved electrical conductivity, the 1T phase usually shows a larger interlayer spacing than the 2H phase, resulting in faster ion diffusion rates and smaller volume changes during cycling.[90,91] Bai *et al.* prepared the 1T-MoS_2/C composite for Li^+ storage. The prepared 1T-MoS_2 not only exhibits metallic conductivity but also shows an expanded interlayer spacing of 0.94 nm (Fig. 2e).[31] The enlarged interlayer space of 1T-MoS_2 compared to that of 2H-MoS_2 (0.62 nm, Fig. 2f) enables rapid intercalation and extraction of Li^+ and buffers the volume changes, leading to improved electrochemical performance. The 1T-WS_2 nanoflowers (NFs) with an enlarged interlayer spacing of 0.67 nm (0.62 nm for 2H-WS_2)

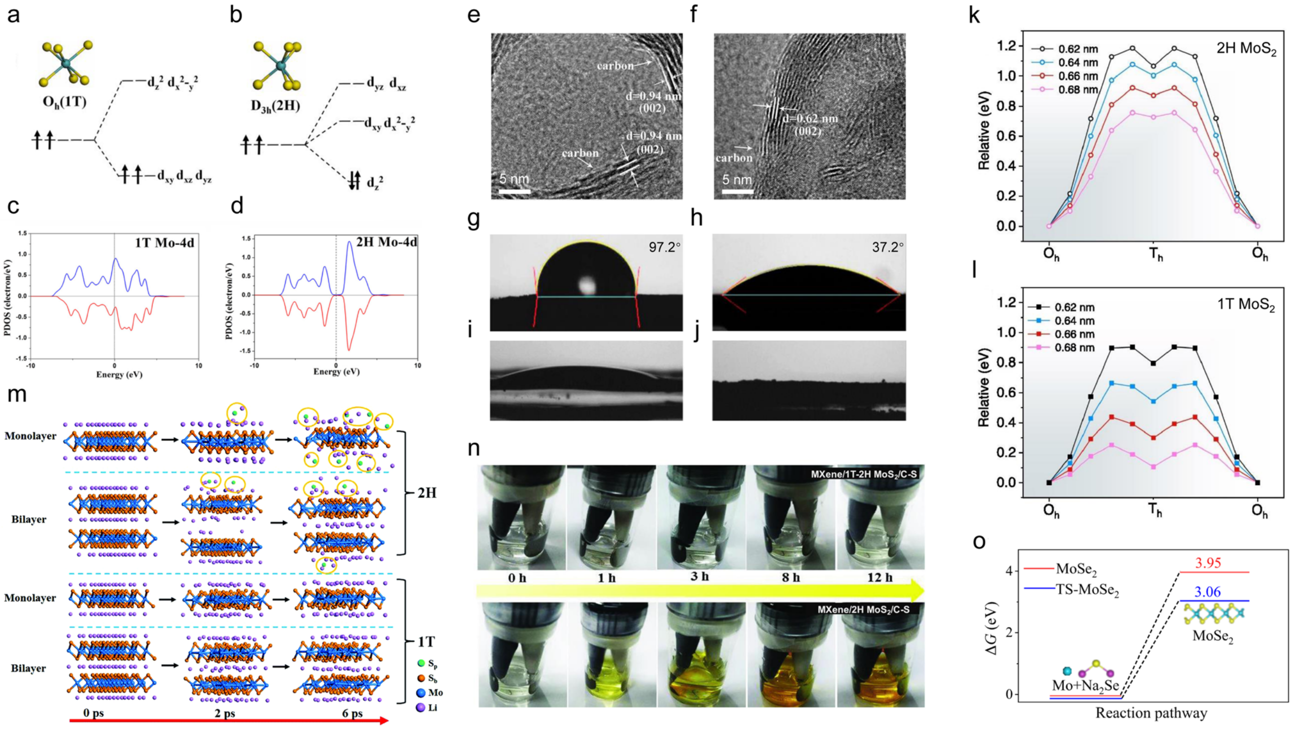

Fig. 2 Electronic structure manipulation of the Mo 4d orbitals as a key to transition from a semiconducting to a metallic phase for Mo-based dichalcogenides. (a and b) The occupation of electrons in Mo 4d orbitals under the crystal fields of the 1T phase and 2H phase. Calculated PDOSs of 4d states of Mo for the (c) 1T phase and (d) 2H phase. HRTEM images of the (e) 1T-MoS_2/C hybrid and (f) 2H-MoS_2/C hybrid. Water contact angle measurements of (g) 3DG/2H-MoS_2 and (h) 3DG/1T-MoS_2. Electrolyte contact angle measurements of (i) 3DG/2H-MoS_2 and (j) 3DG/1T-MoS_2. Calculated energy profiles of Zn^{2+} diffusion in (k) 2H phase and (l) 1T phase MoS_2 with different interlayer distances. (m) Snapshots of trajectories for lithiated 2H-MoS_2 monolayer, 2H-MoS_2 bilayer, 1T-MoS_2 monolayer, and 1T-MoS_2 bilayer nanosheets following 6 ps *ab initio* molecular dynamics (AIMD) simulations at 300 K. (n) Digital photos of glass vials with the MXene/1T–2H MoS_2–C–S and MXene/2H MoS_2–C–S batteries as discharge time increases (0.05C). (o) The ΔG values per formula unit of the reaction between Na_2Se/Mo and $MoSe_2$ under strained and unstrained conditions. Reproduced with permission from: (a–d) ref. 88. Copyright 2015, AIP Publishing; (e and f) ref. 31. Copyright 2019, Wiley-VCH; (g–j) ref. 96. Copyright 2019, Royal Society of Chemistry; (k and l) ref. 97. Copyright 2022, Elsevier; (m) ref. 102. Copyright 2016, Royal Society of Chemistry; (n) ref. 103. Copyright 2018, Wiley-VCH; (o) ref. 113. Copyright 2022, Springer Nature.

also exhibit better electrochemical performance than the 2H-WS_2 NFs and 2H-WS_2 sheets.[92]

When used as aqueous metal-ion battery electrodes, 1T-MoS_2 shows higher hydrophilicity than 2H-MoS_2, which is beneficial for wetting the electrolytes and increasing the ion diffusion rate.[93–95] The water contact angle measurements of three-dimensional graphene (3DG)/2H-MoS_2 and 3DG/1T-MoS_2 are shown in Fig. 2g and h.[96] 3DG/2H-MoS_2 shows a contact angle of 97.2°, which is much higher than 37.2° of 3DG/1T-MoS_2, suggesting that 1T-MoS_2 is highly hydrophilic. Liu *et al.* synthesized MoS_2 nanosheets with different 1T phase contents for aqueous zinc ion storage.[97,98] Because of the high conductivity and hydrophilicity of 1T-MoS_2, a tendency is observed that the electrochemical performance improves with increasing the content of the 1T phase, and the MoS_2 nanosheets with the highest content of the 1T phase exhibit the best electrochemical performance. The density functional theory (DFT) calculations showed that 1T-MoS_2 always exhibits lower Zn^{2+} diffusion energy barriers than 2H-MoS_2 under the same interlayer spacing conditions (Fig. 2k and l).[97] In addition to its high hydrophilicity, 1T-MoS_2 also exhibits better organic electrolyte wettability (Fig. 2i) than 2H-MoS_2 (Fig. 2j).[96]

Moreover, during the conversion reaction process, taking MoS_2 as an example, the formation of polysulfides is unavoidable, resulting in the loss of active materials and the shuttle effect.[34,99] This phenomenon can be mitigated by converting 2H-MoS_2 to 1T-MoS_2 due to the latter's strong adsorption toward polysulfides and higher chemical stability.[100,101] As shown in Fig. 2m, the continuous release of S atoms from 2H-MoS_2 and the formation of polysulfides within 6 ps are evident for both monolayer and bilayer nanosheets from the AMID simulations.[102] In contrast, no S atoms are released from 1T-MoS_2 within 6 ps for both monolayer and bilayer nanosheets, demonstrating the higher chemical stability of 1T-MoS_2 compared to 2H-MoS_2. Furthermore, a polysulfide adsorption experiment was carried out under continuous discharge conditions (Fig. 2n).[103] For the MXene/1T–2H MoS_2–C–S nanohybrids, almost no change in the color of the electrolyte is observed during the 12 h discharging process. However, in the case of MXene/2H MoS_2–C–S nanohybrids, the color of the electrolyte changes from colorless to faint yellow within the first 3 h. Subsequently, the color of the electrolyte changes to dark yellow until the end of the discharge. Therefore, the strong adsorption of 1T-MoS_2 toward polysulfides enables it to have excellent cycling stability and behave as a promising S host. Zhang *et al.* prepared MXene/1T–2H MoS_2–C nanohybrids as an S host for Li–S batteries.[103] Compared to the MXene/2H MoS_2–C host, the MXene/1T–2H MoS_2–C–S electrode exhibits better cycling stability.

Phase engineering is a very effective strategy to improve the dynamic properties and electrochemical performance of Mo and W-based dichalcogenides, and many methods have demonstrated the successful preparation of their 1T phases.[104] The relatively lower temperature hydrothermal/solvothermal methods are often used to prepare 1T phase-containing Mo and W-based dichalcogenides.[105,106] When increasing the reaction temperature or annealing the 1T phase at a high temperature, the 2H phase can be obtained. For example, 1T-MoS_2 can be prepared by a hydrothermal reaction below 200 °C. When the reaction temperature is increased to 240 °C, only the 2H phase exists due to its higher thermodynamic stability.[88] More specifically, when performing hydrothermal/solvothermal reactions or other phase engineering strategies, foreign species intercalation,[107,108] vacancy and dopant introduction,[109,110] exfoliation-restacking,[111,112] *etc.*, are the main pathways for manipulating the Mo 4d electronic structures. Among these, foreign species (such as organic compounds) intercalation not only results in the formation of the 1T phase but can also regulate the Gibbs free energy of the redox reaction by using the strain. For example, Jiang *et al.* reported tensile-strained $MoSe_2$ (TS-$MoSe_2$) using 2-methylimidazole (2-MI) as a scaffold.[113] The introduction of 2-MI not only results in the formation of 1T-$MoSe_2$ but also reduces the Gibbs free energy of the redox chemistry (Fig. 2o), resulting in highly reversible sodium ion storage.

Since the 1T phase has many advantages, the phase transition ratio therefore becomes a very important parameter for the phase engineering strategy. From the viewpoint of thermodynamics, the 1T phase is metastable, and the 2H phase is more stable.[114] Therefore, it is hard to achieve a 100% phase transition for Mo and W-based dichalcogenides. Currently, most TMDs constructed by phase engineering strategies contain around 70% of the 1T phase (Table 3).[36,37,115,116] Although the electrochemical performance of these TMDs has been greatly improved, the construction of pure 1T phase Mo and W-based dichalcogenides is still desirable. He *et al.* reported that they induced a 100% phase transition of MoS_2 from the 2H phase to the 1T phase by electron-injection-engineering.[35] During the synthesis process, the reducing gases generated by the decomposition of melamine donate electrons to the MoS_2 precursor, triggering the formation of pure 1T phase MoS_2. Meanwhile, the TiO nanoparticles generated from the reduction of TiO_2 are chemically bonded with 1T-MoS_2, which ensures the stability of the 1T phase. In addition, a very interesting phenomenon was reported by Ding *et al.* where high magnetic fields can also induce the formation of pure 1T phase MoS_2 and WS_2.[33] They found that 1T-MoS_2 and 1T-WS_2 can be prepared by magneto-hydrothermal processing under magnetic fields of 8 T and 9 T, respectively.

In short, phase engineering can improve the electrical conductivity of Mo and W-based TMDs. Additionally, a larger interlayer spacing, better electrolyte wettability, and stronger polysulfide adsorption are also beneficial for rapid ion storage and stable cycling performance.

3.2 Defect engineering

Generally, ions insert into defect-free TMDs from the edges and diffuse along the interlayers.[117,118] The limited active sites and long diffusion paths are not beneficial for rapid ion storage, resulting in sluggish ion transport kinetics. Defects have been found to be able to increase the active adsorption sites, enhance the conductivity, improve the reactive kinetics, and create additional ion diffusion paths,[55,119–121] which can effectively alleviate the problems faced by defect-free TMDs.

According to the dimensions, the defects in TMDs can be divided into four main types: zero-dimensional (0D) point defects, one-dimensional (1D) line defects, two-dimensional (2D) planar defects, and three-dimensional (3D) volume defects.[122] Among them, the 0D point defects are more favorable due to their positive effects on the electrochemical performance and their easy and controllable incorporation.[123] Therefore, point defects will be mainly discussed in this section. For example, as shown in Fig. 3a–h,[124] the most commonly observed point defects in monolayer MoS_2 include the monosulfur

Table 3 Summary of the ratios of the 1T phase prepared by different phase engineering strategies

Materials	Methods	1T phase ratio (%)	Ref.
MoS_2	Hydrothermal method: 160 °C for 24 h	51	97
$MoSe_2$	Hydrothermal method: 200 °C for 12 h	53.7	115
MoS_2	Hydrothermal method: 180 °C for 24 h + solvothermal method: 200 °C for 8 h	60	116
$MoSe_2$	Solvothermal method: 220 °C for 24 h	65	36
MoS_2	Solvothermal method: 200 °C for 12 h	62.5	106
MoS_2	Solvothermal method: 180 °C for 20 h	69.1	37
MoS_2	Exfoliated and restacked method	70	93
MoS_2	Hydrothermal method: 160 °C for 24 h	70	98
$MoSe_2$	Solvothermal method: 220 °C for 48 h	78.6	90
$MoSe_2$	Plasma-assisted annealing method	91	109
MoS_2	Solvothermal method: 210 °C for 24 h + annealing method:700 °C for 2 h	100	35
MoS_2 + WS_2	Magneto-hydrothermal method	100	33

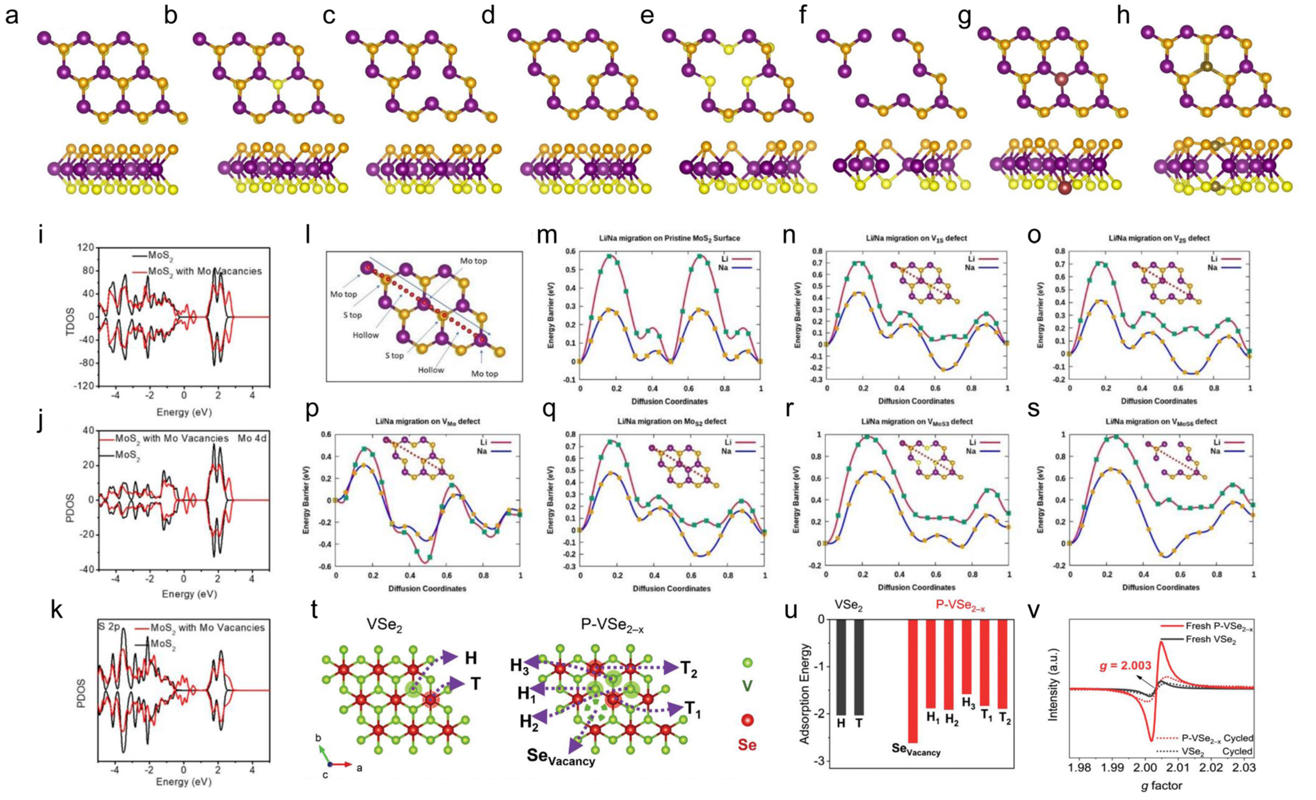

Fig. 3 Optimized geometry of various defects in monolayer MoS$_2$. (a) Pristine MoS$_2$, (b) V_{1S}, (c) V_{2S}, (d) V_{Mo}, (e) V_{MoS3}, (f) V_{MoS6}, (g) Mo_{S2}, and (h) $S2_{Mo}$ vacancies. The purple and yellow colored balls denote Mo and S atoms, respectively. The top layer of S atoms is in golden yellow color, and the bottom layers are in light yellow color. In the Mo_{S2} vacancy, the maroon-colored ball represents the antisite Mo substituting a sulfur atom. In the $S2_{Mo}$ vacancy, the gray ball represents the antisite S substituting a Mo atom. The diffusion path for Li/Na on MoS$_2$ with defects. Total (i) and partial (j and k) charge density of states of MoS$_2$ with Mo vacancies and pristine MoS$_2$. Diffusion energy profiles for Li/Na diffusion barriers for (l) pristine MoS$_2$, (m) Li/Na migration path on pristine MoS$_2$, (n) monosulfur vacancy, (o) disulfur vacancy, (p) Mo vacancy, (q) Mo_{S2} vacancy, (r) MoS3 vacancy, and (s) MoS6 vacancy. (t) K^+ adsorption sites on VSe$_2$ and P–VSe$_{2-x}$, and (u) their corresponding adsorption energies. (v) EPR spectra of VSe$_2$ and P–VSe$_{2-x}$ electrodes before and after one galvanostatic charge–discharge cycle. Reproduced with permission from (a–h and l–s) ref. 124. Copyright 2019, American Chemical Society; (i–k) ref. 126. Copyright 2019, American Chemical Society; (t–v) ref. 42. Copyright 2023, Wiley-VCH.

vacancy (V_{1S}), disulfur vacancy (V_{2S}), Mo vacancy (V_{Mo}), vacancy complex V_{MoS3} (V_{MoS6}) of Mo and nearby three (six) sulfur, and two types of antisite defects where the Mo atom substitutes an S2 column (Mo_{S2}) or an S2 column substitutes a Mo atom ($S2_{Mo}$). The formation energies of various vacancies are listed in Table 2, from which it can be observed that the formation energies of V_{1S}, V_{2S}, and V_{Mo} are lower than those of the other vacancies, implying that they are easier to form and are more widely studied.[122,123] In addition, it is worth pointing out that although the defect engineering strategies reported below claim that TMD electrodes containing anionic or cationic vacancies can be controllably synthesized, the preparation of TMD electrodes containing only specific types of defects has not yet been reported.

By manipulating the electronic structures of the Mo 4d orbitals, the conversion of Mo-based TMDs from a semiconducting phase to a metallic phase was achieved *via* phase engineering, leading to a great improvement of conductivity and electrochemical performance. The presence of defects can also manipulate the electronic structures of the Mo 4d orbitals. Due to the presence of defects, the localized electrons generate midgap states within the valence or conduction bands, resulting in p-type or n-type conductors. The midgap states generate free charge carriers, thereby enhancing the conductivity.[125] As shown in Table 4, pristine MoS$_2$ exhibits a direct bandgap of around 1.67 eV. When different defects are created, the bandgap decreases to varying degrees, indicating enhanced conductivity. For example, Liang *et al.* reported nitrogen-doped carbon nanofiber@MoS$_2$ nanosheet arrays with sulfur vacancies for Na^+ storage.[41] The introduction of sulfur vacancies enhances the conductivity of the materials and serves as the new active site for adsorbing Na^+. Therefore, the charge transfer resistance is reduced, and the specific capacity and rate performance are improved. Li *et al.* developed a hollow microcube framework composed of ultrathin MoS$_2$ nanosheets rich in Mo vacancies.[126] Theoretical calculations reveal that the Mo vacancies can improve the electrical conductivity of MoS$_2$ due to the narrowed bandgap (Fig. 3i–k) and the enhanced interaction between MoS$_2$ and Na, resulting in rapid reaction kinetics and improved Na storage capacity.

Table 4 The calculated vacancy formation energy (eV), energy gap (eV), adsorption energies (E_{ad}), and barrier heights (eV) of pristine and various types of defective MoS_2

Vacancy	Vacancy formation energy (eV)	Energy gap E_g (eV)	Adsorption energy for Li $E_{ad\text{-}Li}$ (eV)	Adsorption energy for Na $E_{ad\text{-}Na}$ (eV)	Barrier height for Li (eV)	Barrier height for Na (eV)
Pristine MoS_2	—	1.67	−2.08	−1.28	0.57	0.28
V_{1S}	1.95	1.06	−2.57	−1.99	0.69	0.43
V_{2S}	3.78	1.02	−2.44	−1.89	0.70	0.40
V_{Mo}	5.73	0.09	−3.92	−1.81	0.46	0.32
V_{MoS3}	7.90	0.64	−2.83	−2.09	0.91	0.65
V_{MoS6}	13.89	0.03	−3.37	−2.28	0.95	0.67
MoS_2	6.89	0.01	−2.58	−1.99	0.74	0.47
$S2_{Mo}$	9.33	0.48	−2.28	−1.60	—	—

In addition, the presence of defects in TMDs is believed to be able to provide stronger binding sites for alkali metal atoms. The adsorption energies for Li and Na at the top site (above the top of a Mo atom) of pristine MoS_2 and at the seven defective regions are listed in Table 4.[124] It can be observed that pristine MoS_2 shows a Li adsorption energy of −2.08 eV and a Na adsorption energy of −1.28 eV. When different defects are created, the adsorption energies for Li and Na are higher than that of pristine MoS_2. The high adsorption energies of various defects indicate the easy binding and the favorable chemical interaction between Li/Na and defective MoS_2. Besides the adsorption energies, the diffusion kinetics are also important for the electrochemical reaction rate. As shown in Fig. 3l–s, the associated activation energy barriers of pristine MoS_2 and all types of defects were calculated with the fixed path.[124] For the pristine MoS_2 model, the path features two symmetrical absolute maxima, two symmetrical local maxima, and two local minima for the diffusion barriers when Li and Na pass through the two-unit cell (Fig. 3m). Consistent with the diffusion path of pristine MoS_2, only one maximum is found in the vicinity of the defects (Fig. 3n–s), as the barrier height disappears in the defect regions. Thus, it is clear that the presence of vacancies reduces the barrier height in the defective regions, and Li^+ and Na^+ can diffuse efficiently into the vacancy regions and then diffuse across the vacancies to the top site of the next cell in the MoS_2 plane (Fig. 3n–p). Although the introduction of vacancies enhances the barrier energies in the vicinity of the defects (Table 4), the barrier energies near 0.7 eV and 0.4 eV are believed to ensure the rate performance of LIBs and NIBs at room temperature. The enhanced adsorption energies of V_{MoS3} and V_{MoS6} essentially act as traps, which inhibits the atomic motion of Li^+ and Na^+ (Fig. 3r and s). The presence of antisite defects also promotes the migration of Li and Na atoms on the defective MoS_2 surface (Fig. 3q). However, in the case of antisite defect $S2_{Mo}$, the migration of both Li and Na ions ceases because the migrating Li^+ and Na^+ are repelled by the sulfur atoms replacing the Mo atoms. A systematic study is still lacking for the adsorption and diffusion properties of K^+ in pristine and defective MoS_2.

The presence of defects can enhance the conductivity and provide stronger and more binding sites, which is very beneficial for electrochemical performance. However, for those TMDs that undergo conversion reactions during cycling, the crystal structures experience a reconstruction process, which may be detrimental to the retention of defects. Sha *et al.* explored the role of anion vacancies of VSe_2 in K^+ storage.[42] They found that the existence of anion vacancies in VSe_2 can promote the electrochemical reaction kinetics. In addition, the defect regions provide more active sites (Fig. 3t), and they all exhibit large K^+ adsorption energies (Fig. 3u). However, the anion vacancies in VSe_2 are found to influence the first potassiation process primarily. In the subsequent cycles, they disappear and cannot be regenerated, which is demonstrated by electron paramagnetic resonance (EPR) (Fig. 3v). Although the vacancies in VSe_2 disappear after the first cycle, the electrochemical performance of defective VSe_2 is still much better than that of pristine VSe_2, which is interesting and needs further exploration. In the case of those TMDs that only undergo intercalation and extraction reactions, the defects may be preserved well during cycling. Liu *et al.* reported a TiS_2 anode rich in cation vacancies, which only experiences intercalation and extraction reactions during cycling.[127] *Ex situ* EPR spectra demonstrate that, even after 60 cycles, the EPR signal of defective TiS_2 is almost unchanged, indicating that the defects were well retained. Still, much work is needed to determine the clear relationship between the reaction types and defect retention.

It is believed that introducing defects will bring new ion diffusion pathways, thus enhancing the electrochemical reaction kinetics. An experiment designed by Zhang *et al.* demonstrated that small-size ions can also intercalate through the top surface of few-layer defective MoS_2 apart from the edges (Fig. 4a).[128] The color changes of MoS_2 flakes with sealed and open edges during cycling indicate that Li^+ can both intercalate through the top surface and the edges (Fig. 4b), and the process of intercalating through the top surface of MoS_2 flakes has much better reversibility. In the case of Na^+ storage (Fig. 4c and d), the MoS_2 flakes with sealed and open edges both exhibit excellent reversibility, although the ionic radius of Na^+ is higher than that of Li^+. This phenomenon is attributed to the relatively weak chemical binding between Na and MoS_2.[129] In contrast, no obvious change is observed when attempting to intercalate K^+ into sealed MoS_2, indicating that K^+ cannot intercalate through the top surface of defective MoS_2 flakes (Fig. 4e and f). The color changes of K^+ intercalated into MoS_2 flakes with open edges are similar to that of Li^+, indicating that the reversibility of this process is also poor. These observations demonstrate that the

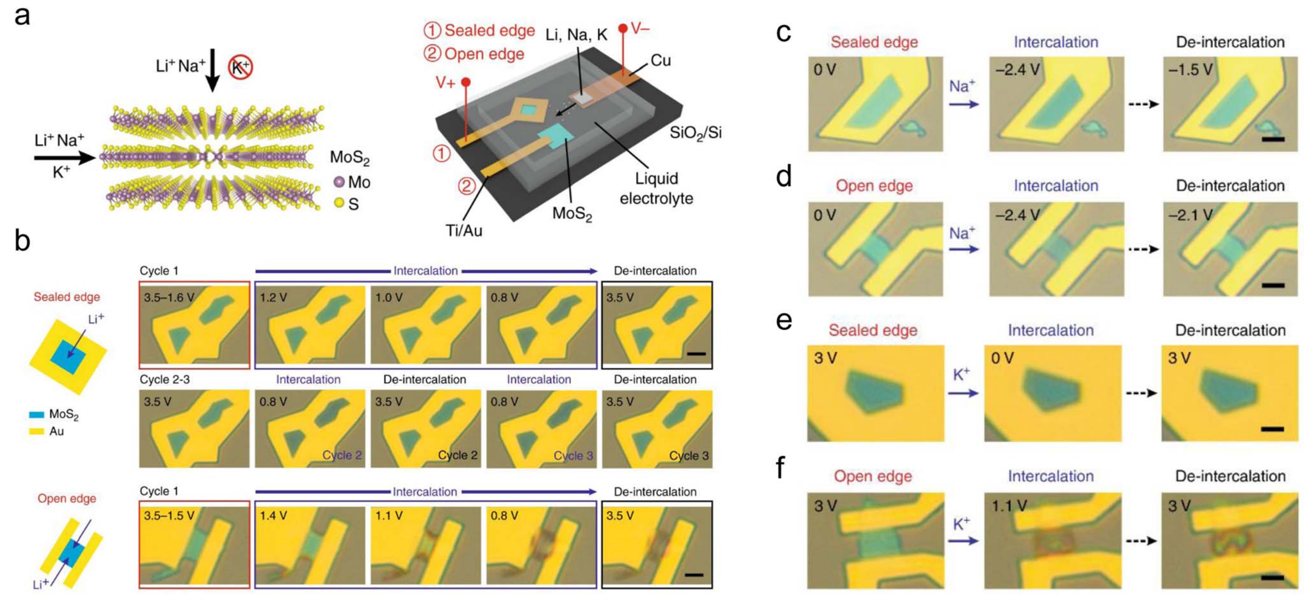

Fig. 4 Schematic representation of MoS_2 and of the experimental setup to study intercalation and de-intercalation. (a) Li^+, Na^+, and K^+ intercalation into MoS_2 through top and edge channels. An electrochemical cell is used to perform intercalation of Li^+, Na^+, and K^+ into MoS_2 with sealed and open edges. (b) *In situ* optical microscopy images of Li intercalation into MoS_2 through top surface and edges, respectively. Scale bars, 5 μm. (c and e) *In situ* optical microscopy images of Na and K intercalation into MoS_2 through the top surface. (d and f) *In situ* optical microscopy images of Na and K intercalation into MoS_2 through the edges. Scale bars in (c–f), 5 μm. Reproduced with permission from ref. 128. Copyright 2018, Springer Nature.

defects on the top surface of MoS_2 allow the intercalation of small-size ions (such as Li^+ and Na^+) but reject large-size ions (such as K^+). Similarly, additional 3D ion diffusion pathways have also been explored through theoretical or experimental studies.[40,42]

The large charge density of multivalent ions leads to a high ion intercalation and diffusion impedance in TMDs. Introducing defects can enhance the electrochemical reaction kinetics of TMDs, thus improving their storage capacity for multivalent ions. Xu *et al.* activated MoS_2 for Zn^{2+} storage by introducing sulfur vacancies.[44] Compared to pristine MoS_2, MoS_2 with sulfur vacancies exhibits much greater capacity, better rate performance, as well as high capacity retention. Theoretical calculations reveal that the numerous defects act as the preferential intercalation sites for Zn^{2+} storage. MoS_2 nanosheets with sulfur vacancies were also reported by Zhu *et al.* for Mg^{2+} storage.[130] They showed that introducing defects into MoS_2 nanosheets improves the ability of MoS_2 to store Mg^{2+}. Bai *et al.* used defective VSe_2 for Zn^{2+} storage by introducing selenium vacancies and reported an enhanced electrochemical performance.[45] By using theoretical calculations, they found that the presence of selenium vacancies adjusts the adsorption energy of Zn^{2+}, which makes the electrochemical reaction more reversible.

In short, introducing defects into TMDs can enhance their conductivity, provide more and stronger binding sites, create new ion transfer pathways, and shorten the diffusion paths of metal ions, which are beneficial for improving the ion storage capacity of TMDs. However, in some TMDs, the defects disappear after the first cycle and cannot be regenerated, yet electrochemical performance improvements can still be observed in the subsequent cycles. This phenomenon is interesting and has not been explained clearly yet. In addition, the clear relationship between the reaction types and defect retention also needs further studies for a better understanding.

3.3 Interlayer spacing expansion

A low ion diffusion barrier is essential for rapid ion transport in TMDs. Although the presence of defects has been demonstrated to accelerate ion diffusion, their positive effects only exist locally.[124] Therefore, a strategy that can comprehensively reduce the ion diffusion barriers of TMDs is needed. It has been reported that although the interlayer spacing of ReS_2 and MoS_2 is very similar (6.14 Å for ReS_2 and 6.15 Å for MoS_2), the diffusion barriers of Li^+ in ReS_2 nanosheets are significantly lower than that in MoS_2 nanosheets,[131] and the main reason is attributed to the much weaker vdW interactions between the adjacent layers in ReS_2 than that in MoS_2.[131,132] The weak vdW interactions between TMD interlayers are beneficial for rapid transport of ions with low impendence. As a result, weakening the vdW interactions between TMD interlayers could be an effective strategy to comprehensively reduce the ion diffusion barriers of TMDs. In addition to selecting some TMDs that exhibit weak vdW interactions on their own, such as ReS_2, a more effective and broadly applicable strategy is to expand the interlayer spacing of TMDs to reduce their vdW interactions.[131,133,134]

The relationship between the interlayer spacing and the diffusion of alkali metal ions in MoS_2 was explored by theoretical calculations.[135,136] With the diffusion pathway of O_h (stable site) → T_h (metastable site) → O_h, the diffusion barriers of Na^+

decrease from 1.14 eV to 0.2 eV with increasing the interlayer spacing from 6.5 Å to 9 Å. In the case of Li^+, with the same diffusion pathway, the diffusion barriers decrease continuously from 0.54 eV with increasing the interlayer spacing from 6.5 Å to 7.5 Å. When the interlayer spacing is larger than 7.5 Å, the T_h site becomes more stable than the O_h site, making the diffusion from O_h to T_h endothermic.[137,138] Therefore, the diffusion barriers of Li^+ increase slightly to 0.31 eV with increasing the interlayer spacing from 7.5 Å to 9 Å. The relationship between the interlayer spacing and the diffusion of K^+ in MoS_2 was also explored by Zheng *et al.* with the diffusion path shown in Fig. 5a (the diffusion path of K^+ is indicated by the blue dotted line).[136] The results show that the diffusion barriers of K^+ decrease from 3.94 eV to 0.045 eV with increasing the interlayer spacing from 6.2 Å to 9.2 Å (Fig. 5b). In general, taking MoS_2 as an example, the diffusion barriers of alkali metal ions decrease with increasing the interlayer spacing of TMDs, and the increased interlayer spacing is beneficial for the rapid ion transport kinetics of TMDs.[139,140]

Xu *et al.* summarized the strategies for synthesizing interlayer-expanded TMDs as ‘top-down’ and ‘bottom-up’ approaches.[133] Specifically, the methods for expanding interlayer spacing can be divided into two categories: one is the restacking of exfoliated TMD monolayer nanosheets, and the other is to introduce guests or guest precursors into TMD interlayers.[133,141] Du *et al.* restacked MoS_2 by an exfoliation and restacking process with enlarged interlayer spacing. The enlarged interlayer spacing of MoS_2 provides a larger space for Li^+ intercalation and reduces the diffusion barriers of Li^+. Consequently, the restacked MoS_2 exhibits improved electrochemical performance compared to raw MoS_2.[142] In the case of introducing guests or guest precursors into TMD interlayers, they include many foreign species, such as ions, organics, carbon, *etc.*[133,143–145] The intercalated ions are often metal ions and NH_4^+.[137,146,147] Zak *et al.* intercalated alkali metals into MS_2 (M = W and Mo) nanoparticles by exposing MS_2 to alkali metal (Na and K) vapor, and observed a substantial increase (≈3–5 Å) in the interlayer spacing of the intercalated phase.[146] Ma *et al.* reported a multivalent ion intercalation method to construct 3D Co–MoS_2 nanoflowers with expanded interlayer spacing. The intercalated Co^{2+} forms S–Co–S covalent bonds and enlarges the maximum interlayer spacing to 1.1 nm, which dramatically reduces the diffusion barriers of Na^+.[141] Hu *et al.* expanded the interlayer spacing of MoS_2 by intercalating Na^+ and NH_4^+. The expanded interlayers reduce the charge transfer resistance and provide more active sites for Na^+ storage.[147] As for the organic

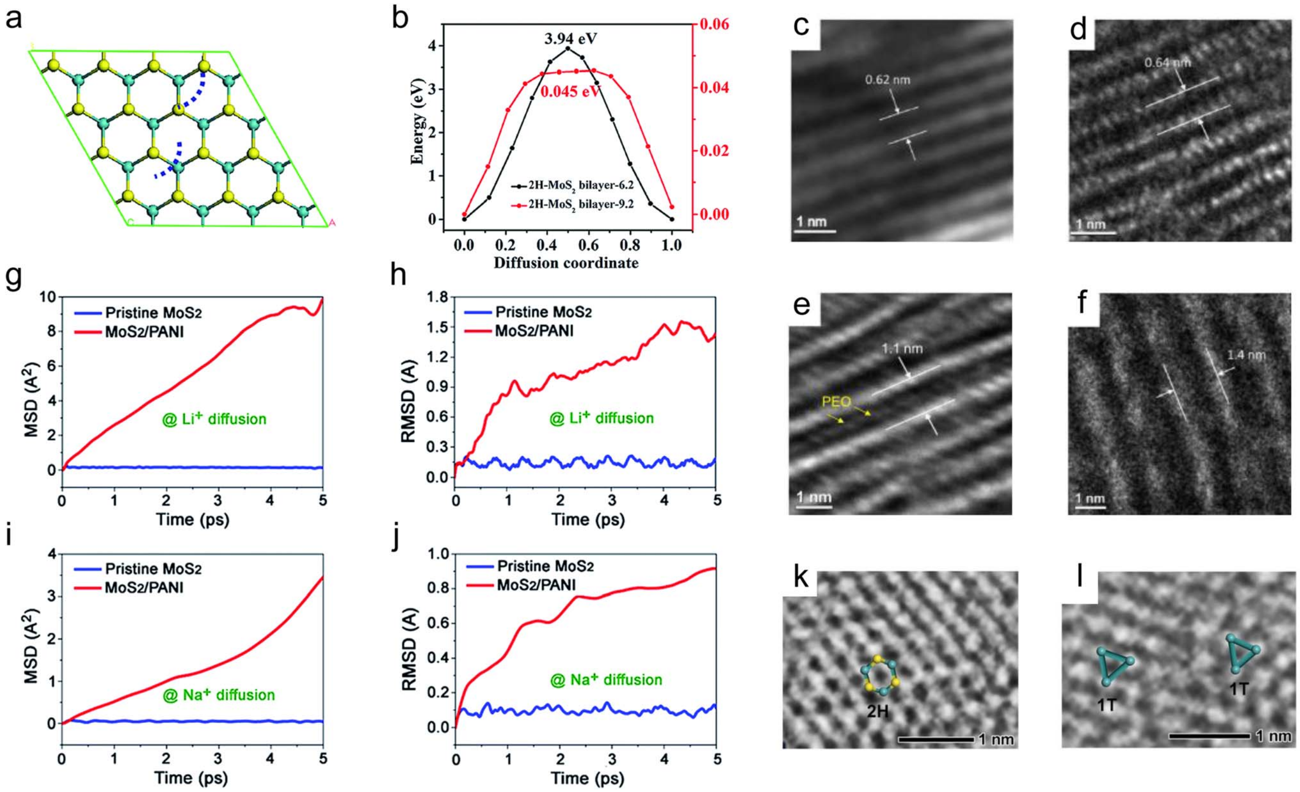

Fig. 5 Interlayer spacing and diffusion of alkali metal-ions. (a) Top view of the optimized MoS_2/MoS_2 interface (the blue dotted line indicates the K^+ diffusion path). (b) Energy profiles along the diffusion path in the selected interlayer spacing of MoS_2/MoS_2. (c and e) The mean square displacement and (d and f) the root mean square displacement of Li^+/Na^+ as a function of time of Li^+/Na^+ diffusion on the pristine MoS_2 nanosheets and the MoS_2/PANI hybrid nanosheets. (g–j) High-resolution TEM images show the cross-sectional view of com-MoS_2, re-MoS_2, PEO_{1L}–MoS_2, and PEO_{2L}–MoS_2. High-resolution TEM images and atomic models for (k) 2H-MoS_2 and (l) 1T-MoS_2, respectively. Reproduced with permission from (a and b) ref. 136. Copyright 2019, Royal Society of Chemistry; (c–f) ref. 46. Copyright 2017, Royal Society of Chemistry; (g–j) ref. 151. Copyright 2015, Elsevier; (k and l) ref. 149. Copyright 2020, Wiley-VCH.

guests, a large number of organics has been reported that can be intercalated into TMD interlayers,[14,145] such as poly(ethylene oxide) (PEO), polyaniline (PANI), oleylamine, methylamine, polypyrrole, *etc.*[46,47,148–150] Yao and co-workers synthesized PEO-intercalated MoS_2 composites (PEO–MoS_2) using an exfoliation-restacking method.[151] They prepared 4 samples, commercial MoS_2 (com-MoS_2), restacked MoS_2 without PEO (re-MoS_2), and monolayer and bilayer PEO-intercalated MoS_2 composites (PEO_{1L}–MoS_2 and PEO_{2L}–MoS_2) for comparison. The com-MoS_2 shows a sharp diffraction peak located at 14.4°, corresponding to an interlayer spacing of 0.62 nm (Fig. 5c). For re-MoS_2, PEO_{1L}–MoS_2, and PEO_{2L}–MoS_2, the peaks become broadened and shift to lower angles, indicating the less ordered structures and the larger interlayer spacing. Compared to that of com-MoS_2, the interlayer spacing of re-MoS_2, PEO_{1L}–MoS_2, and PEO_{2L}–MoS_2 is increased to 0.64 nm, 1.1 nm, and 1.4 nm, respectively (Fig. 5d–f). As a result, PEO_{2L}–MoS_2, with a 160% increase in the interlayer spacing, exhibits the best electrochemical performance due to its greatest improvement in Na^+ diffusivity. It is worth pointing out that the addition of excessive PEO will not further increase the interlayer spacing of MoS_2. The incorporation of a conducting polymer can not only increase the interlayer spacing but also improve the conductivity of TMDs. Wang *et al.* prepared MoS_2/polyaniline (PANI) hetero-structures with enlarged interlayer spacing for Li^+ and Na^+ storage,[46] and they performed an AIMD simulation of the diffusion of Li^+ and Na^+ on pristine MoS_2 nanosheets and the MoS_2/PANI hybrid nanosheets (Fig. 5g–j). The mean square displacement (MSD) and the root mean square deviation (RMSD) values of Li^+ and Na^+ in MoS_2/PANI hybrid nanosheets are both much larger than that in pristine MoS_2 nanosheets, suggesting the faster diffusion mobility of Li^+ and Na^+, which is attributed to the improved conductivity and the enlarged interlayer spacing of MoS_2/PANI composites. In the case of the carbon guests, they are usually formed *via* a subsequent carbonization process of MoS_2 with pre-intercalated organics.[152–154] For example, Jiang *et al.* prepared a 2D MoS_2/mesoporous carbon hybrid nanostructure by annealing the MoS_2/polydopamine (PDA) composites.[155] Feng *et al.* synthesized interlayer-expanded MoS_2/carbon hetero-aerogels by directly intercalating different polymers (polyethyleneimine and polyethylene glycol) into the MoS_2 interlayers before the carbonization process,[156] and the effects of intercalated carbon layers are similar to that of intercalated conducting polymers, such as PANI. In addition, the introduction of foreign species can also induce the phase transformation from the semiconducting phase to the metallic phase, which can enhance the electrical conductivity of Mo and W-based dichalcogenides. Ye *et al.* introduced methylamine into the MoS_2 interlayers.[149] The introduction of methylamine can not only expand the interlayer spacing, but also force the transformation of MoS_2 from the 2H phase to the 1T phase, resulting in the formation of a metal-semiconducting mixed MoS_2 phase (Fig. 5k and l).

The interlayer spacing expansion strategy is also widely used for multivalent ions to enhance their diffusion behaviors in TMDs.[157–160] Similar to the theoretical research of the diffusion behaviors of alkali metal ions in MoS_2, the diffusion behaviors of Mg^{2+} in MoS_2 with varying interlayer spacing were also

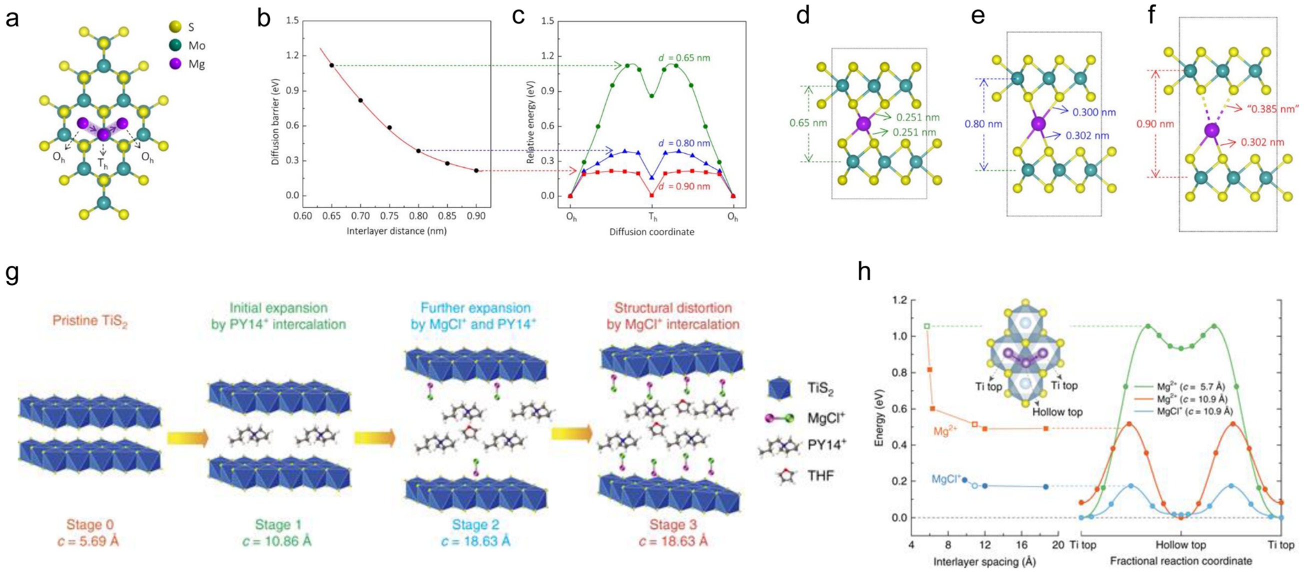

Fig. 6 Mg diffusion in MoS_2 and TiS_2. (a) Calculated Mg diffusion path in MoS_2. (b) The energy barrier for Mg diffusion continuously decreases as the interlayer distance of MoS_2 increases. (c) Potential energy diagram for Mg migration at interlayer spacings of $d = 0.65$, 0.80, and 0.90 nm. As the interlayer distance increases from 0.65 nm (d) to 0.80 nm (e) and then 0.90 nm (f), the bond between Mg and MoS_2 lengthens and is finally broken on one side. (g) A schematic of structural evolution of TiS_2 at different stages of intercalation. (h) First-principles calculations for the diffusion of Mg-ions in TiS_2. The energy barrier for the migration of Mg^{2+} and $MgCl^+$ as a function of the interlayer distance of TiS_2 at the dilute limit. The diffusion path from a Ti top site to another Ti top site *via* the adjacent hollow top site is shown in the inset. Energy diagrams along the diffusion path for the three representative cases of Mg^{2+} at $c = 5.7$ Å (green), Mg^{2+} at $c = 10.9$ Å (orange), and $MgCl^+$ at $c = 10.9$ Å (cyan). Reproduced with permission from (a–f) ref. 161. Copyright 2015, American Chemical Society; (g and h) ref. 162. Copyright 2017, Springer Nature.

explored by Yao and co-workers in the diffusion pathway of $O_h \rightarrow T_h \rightarrow O_h$ (Fig. 6a).[161] As shown in Fig. 6b and c, as the interlayer spacing increases from 0.65 nm to 0.9 nm, the diffusion barriers continuously decrease from 1.12 eV to 0.22 eV. The reason behind the continuous decrease in the diffusion barriers is the gradually weaker bonding between Mg and one of the two layers of MoS_2 (Fig. 6d–f). It is worth pointing out that traditional interlayer engineering uses the TMDs (whose interlayer spacing has already been expanded) as electrode materials, which needs a pre-processing step. Yao and co-workers further developed an *in situ* interlayer expansion strategy for TiS_2 for fast $MgCl^+$ storage *via* electrolyte engineering.[162] As shown in Fig. 6g, they added PY14Cl into the electrolyte, and $Py14^+$ expanded the interlayer of TiS_2 *in situ* first during discharging in stage 1. From stage 1 to stage 3, a large amount of $MgCl^+$ is intercalated continuously with a small amount of THF molecules, resulting in greatly improved electrochemical performance. The theoretical calculations show that for the same interlayer spacing, the diffusion barriers of $MgCl^+$ are always lower than that of Mg^{2+}, indicating the advantage of $MgCl^+$ storage (Fig. 6h). For Zn^{2+} storage, Huang *et al.* intercalated PANI into MoS_2 interlayers to expand the interlayer spacing.[49] The intercalated PANI expands the diffusion channels of Zn^{2+} and reduces the electrostatic interaction between Zn^{2+} and MoS_2, thus enhancing the electrochemical performance. Cui *et al.* introduced anionic organic layers (sodium dodecyl benzene sulfonate) into WSe_2 to form superlattice-type WSe_2 (S-WSe_2) for Al^{3+} storage. The interlayer spacing expansion strategy makes S-WSe_2 more active as a cathode in rechargeable Al batteries.[163]

In short, the interlayer spacing expansion strategy can comprehensively reduce the diffusion barriers of metal-ions in TMDs. The enlarged specific surface, the transformation of TMDs from the semiconducting phase to the metallic phase, the reduced lattice stress, and the improved electrical conductivity of TMDs are also observed.

3.4 Heteroatom doping

Similar to introducing defects into TMDs, heteroatom doping is also an effective strategy to modulate the local properties of TMDs, which has been reported to improve the conductivity, expand the interlayer spacing, and enhance the atom adsorption capacity of TMDs.[164–166] The doped atoms can be divided into two categories: metal heteroatoms, such as Mn, Zn, Fe, Co, Ni, Cu, Re, Pd, Sn, and Au,[50,167–174] and non-metal heteroatoms, such as N, O, As, P, F, Cl, Br, I, H, and B.[51,170,174–176] The dopant type is an important factor that affects the electrochemical performance of TMDs.

Sun *et al.* theoretically investigated the properties of heteroatom-doped monolayer MoS_2 and the adsorption and diffusion of Li on heteroatom-doped MoS_2 by substituting S with some nonmetallic elements (N, P, As, F, Cl, and I) and Mo with some metallic elements (Fe, Co, Ni, Cu, and Zn) (Fig. 7a–f).[177] The DOS of monolayer MoS_2 with different doping elements is shown in Fig. 7a and b. Although the doped monolayer MoS_2 still exhibits semiconducting characteristics, the conductivity is improved to varying degrees. For metallic heteroatom doping, substituting Mo with Co, Ni, Cu, and Zn makes monolayer MoS_2 exhibit p-type conducting behavior. For non-metallic heteroatom doping, substituting S with N, P, and As also makes monolayer MoS_2 exhibit p-type conducting behavior due to their one less valence electron than S. In contrast, substituting S with F, Cl, and I makes monolayer MoS_2 exhibit n-type conducting behavior. In the case of studying the adsorption of Li on heteroatom doped monolayer MoS_2, two types of adsorption sites, the hollow site (H) and the top site above Mo (T), and the position of the adsorption sites as a function of distance from the doped site are considered. The adsorption energies of Li on pristine monolayer MoS_2 are −0.95 and −1.24 eV for H and T sites. For all doped elements studied in this work,[177] higher adsorption energies are observed near the doped sites, indicating the stronger bonding between Li and doped monolayer MoS_2, and the adsorption energies decrease with increasing the distance from the adsorption sites to the doped sites. In addition, for non-metallic heteroatom doping, the adsorption energies of Li on N, P, and As doped monolayer MoS_2 are higher than that on the other three elements (F, Cl, and I) doped monolayer MoS_2, indicating that p-type doping is more beneficial for improving the adsorption of Li. This phenomenon can also be found in the case of metallic heteroatom doping. The diffusion energy barriers of Li on doped monolayer MoS_2 were explored with the diffusion pathways shown in Fig. 7c and e. Similar to the effects of defects, when Li diffuses towards the doped sites, the diffusion energy barriers decrease, especially near the doped sites (Fig. 7d and f). In contrast, the diffusion energy barriers increase when Li diffuses away from the doped sites, suggesting the strong adsorption ability of the doped sites. For diffusion pathways far from the doped sites, the diffusion energy barriers will not be affected by the doped heteroatoms. Similarly, the adsorption and diffusion of alkali metals on heteroatom-doped monolayer TiS_2 were then explored by Tian *et al. via* theoretical calculations (Fig. 7g–j).[178] For the adsorption properties of alkali metals, monolayer TiS_2 doped with C, N, and P (corresponding to p-type doping) exhibits higher adsorption energies (Fig. 7g), which is the same as the results obtained by Sun *et al.*[177] And the adsorption energies of alkali metals on TiS_2 with and without doped heteroatoms follow the order of Li > K > Na, which is thought to be affected by both the atomic radius and electronegativity. With the diffusion pathway shown in Fig. 7h and i, the diffusion energy barriers of alkali metals on heteroatom doped monolayer TiS_2 increase to varying degrees compared to that on pristine monolayer TiS_2 (Fig. 7j). But all of them are less than 0.6 eV, which assures the moderate diffusion kinetics of alkali metals on heteroatom doped monolayer TiS_2. The calculation results also show that the diffusion energy barriers follow the order of K < Na < Li, and this tendency has also been observed in other materials.[179–181]

From the standpoint of theoretical calculations, it can be concluded that heteroatom doping enhances the conductivity and improves the adsorption capacity of TMDs for alkali metals. Although the diffusion energy barriers of alkali metals on TMDs increase, the moderate values can still assure moderate

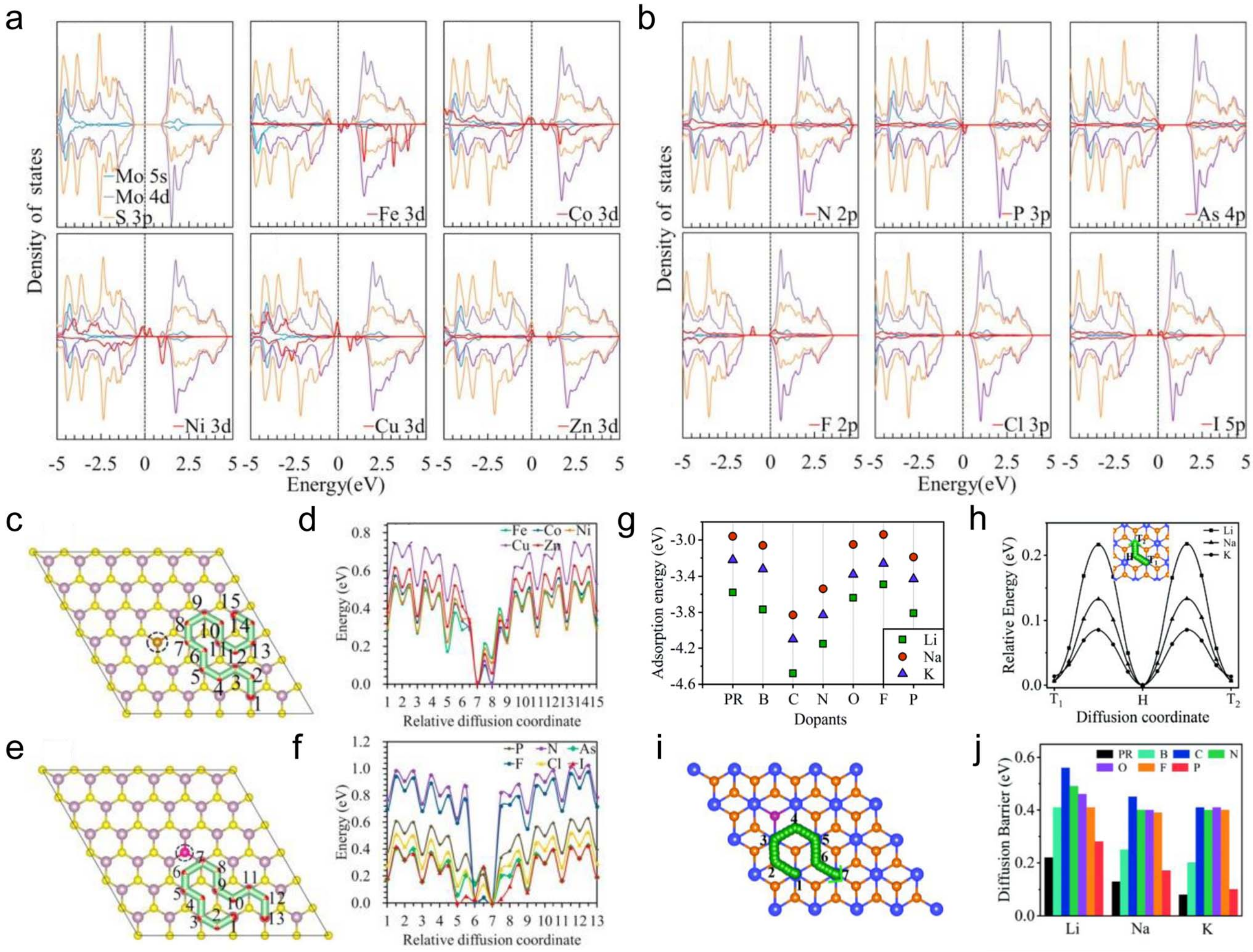

Fig. 7 Density of states, dopant absorption energies, and diffusion pathways. (a) The projected density of states for pristine and monolayer MoS_2 with substitution of Mo with Fe, Co, Ni, Cu, and Zn. (b) The projected density of states for monolayer MoS_2 with substitution of S with N, P, As, F, Cl, and I in monolayer MoS_2. Diffusion path and corresponding diffusion energy profiles for Li on (c and d) metal (e and f) nonmetal atom-doped monolayer MoS_2. (g) The lowest adsorption energies for Li, Na, and K adsorbed on monolayer TiS_2 without and with B, C, N, O, F, and P heteroatom doping. (h) Diffusion pathway and energy profiles for alkali metals on pristine monolayer TiS_2. (i) Diffusion pathway of alkali metals on heteroatom doped monolayer TiS_2. (j) The overall diffusion energy barriers for alkali metals on pristine and heteroatom-doped TiS_2. Reproduced with permission from (a–f) ref. 177. Copyright 2018, American Chemical Society; (g–j) ref. 178. Copyright 2021, Royal Society of Chemistry.

diffusion kinetics. For example, Qin *et al.* developed N-doped MoS_2 nanosheets for Li^+ storage. They found that the N-doped MoS_2 nanosheets exhibit an improved conductivity of *ca.* 1.6×10^{-4} S m^{-1}, while it is only *ca.* 1.1×10^{-5} S m^{-1} for pristine MoS_2 nanosheets.[182] Xie *et al.* prepared Co-doped MoS_2 for Na^+ storage.[183] The Co-doping improves the conductivity of MoS_2 and enhances the adsorption capacity of MoS_2 for Na^+. After being combined with N-doped graphene, Co-doped MoS_2 exhibits higher specific capacity and better rate performance. The doping concentration is an important factor in maximizing the advantages of doping. Zhao *et al.* explored the optimal concentration by injecting different amounts of Mo into VS_2,[184] and 5% Mo-doping concentration exhibits the best electrochemical performance (Fig. 8a and b). Upon further increasing the doping concentrations, the electrochemical performance worsens and is almost the same as that of pristine VS_2. This phenomenon is attributed to the distortion of atomic structures as a result of excessive doping.[185] Apart from the single heteroatom doping, Zhang *et al.* explored NbS_2 nanosheets with varying concentrations of M (M = Fe, Co, Ni) and Se codopants to store Li^+ and Na^+ (Fig. 8c).[186] After optimizing the doping ratios, $Fe_{0.3}Nb_{0.7}S_{1.6}Se_{0.4}$ exhibits the best electrochemical performance. In addition to being able to manipulate the energy band structures of TMDs, the doping of heteroatoms can also lead to the transformation of Mo and W-based dichalcogenides from the semiconducting phase to the metallic phase, which can further enhance the conductivity. Wang *et al.* prepared N-doped MoS_2 for Li storage.[187] And N-doping induces the transformation of MoS_2 from the 2H to the 1T phase (Fig. 8d), thus enhancing the conductivity of MoS_2. He *et al.* developed a plasma-assisted method to introduce highly concentrated P-doping to trigger the phase transformation of $MoSe_2$.[109] The Se vacancies (V_{Se}) induced by plasma treatment lead to the low crystallinity and structural instability of 2H-

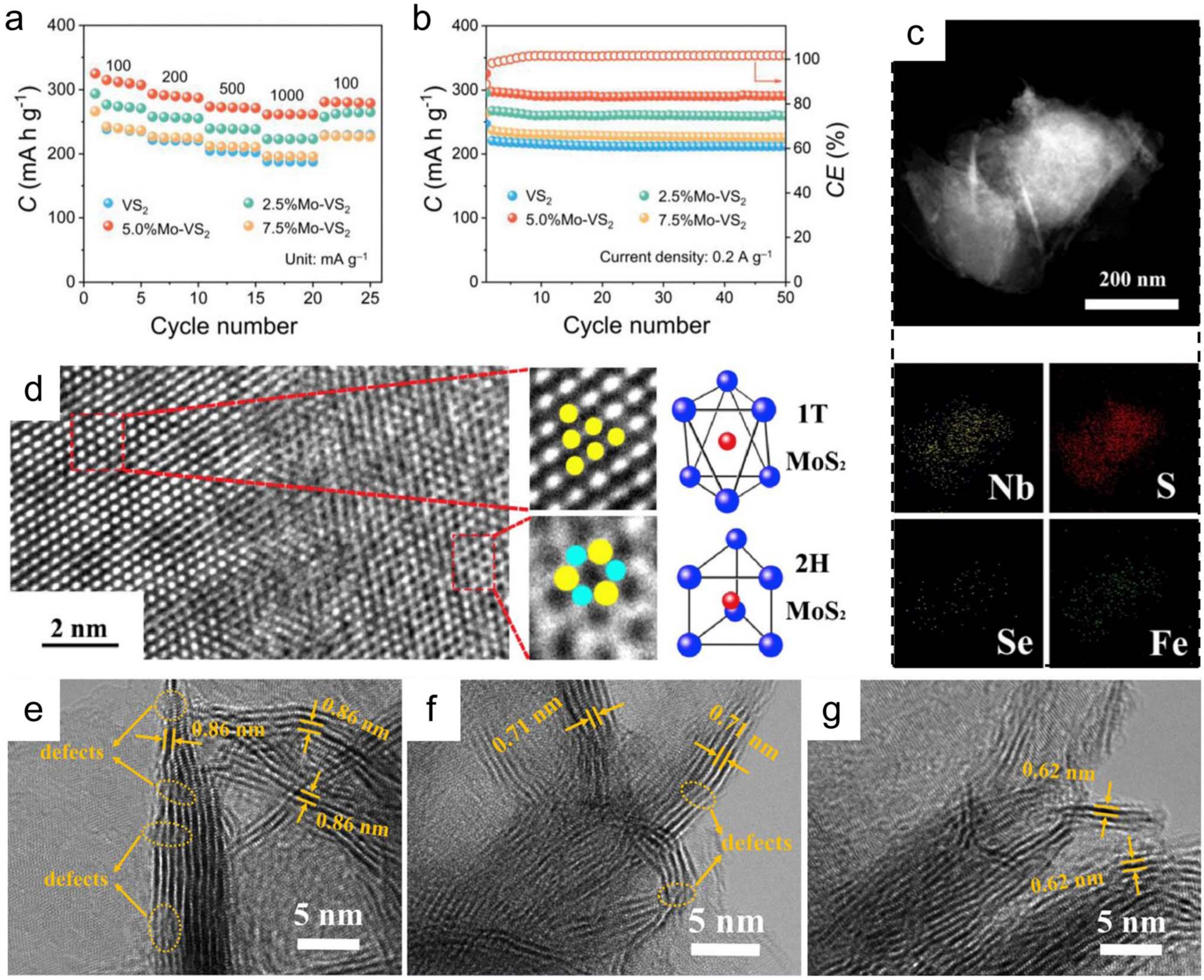

Fig. 8 Electrochemical performance and role of dopants. (a) Rate capability for bare VS_2, 2.5% Mo–VS_2, 5.0% Mo–VS_2, and 7.5% Mo–VS_2 cathodes at 0.1–1.0 A g^{-1}. (b) Cycling performance for bare VS_2, 2.5% Mo–VS_2, 5.0% Mo–VS_2, and 7.5% Mo–VS_2 cathodes at 0.2 A g^{-1}. (c) Mapping of $Fe_{0.3}Nb_{0.7}S_{1.6}Se_{0.4}$ nanosheets. (d) High-resolution TEM images of the synthetic composite and simulated image of (up) 1T and (down) 2H-MoS_2 (S, blue; Mo, red). High-resolution TEM images of N-doped 1T-MoS_2 (e), pure 1T-MoS_2 (f), and pure 2H-MoS_2 (g). Reproduced with permission from (a and b) ref. 184. Copyright 2023, Wiley-VCH; (c) ref. 186. Copyright 2017, American Chemical Society; (d) ref. 187. Copyright 2017, Elsevier; (e–g) ref. 188. Copyright 2021, American Chemical Society.

$MoSe_2$, which decreases the energy barriers of phase transformation and initializes the phase transformation process. Then, the high concentration of P-doping induced by V_{Se} prefers to donate electrons to Mo than Se, thereby triggering and stabilizing the formation of 1T phase $MoSe_2$ with a high transition efficiency of 91%.

For multivalent ion storage, Sheng *et al.* prepared N-doped 1T phase MoS_2 for aqueous Zn^{2+} batteries.[188] Although 1T-MoS_2 exhibits a larger interlayer spacing than 2H-MoS_2 (Fig. 8f and g), they found that N-doping could further increase the interlayer spacing of 1T-MoS_2 (Fig. 8e), thus effectively decreasing the diffusion barriers of Zn^{2+} in MoS_2. Li *et al.* introduced O-doping and defects into MoS_2 for Zn^{2+} storage.[52] O-doping increases the interlayer spacing and cooperates with structural defects to induce the transformation of MoS_2 from the 2H phase to the 1T phase,[51] resulting in improved Zn^{2+} diffusion kinetics, hydrophilicity, and conductivity of MoS_2.

In short, heteroatom doping can enhance the conductivity, improve the metal adsorption ability, induce phase transformation, and expand the interlayer spacing of TMDs. Different types of doping exhibit different effects.

3.5 Alloy engineering

TMD alloys have been the subject of active research in energy conversion and storage. Unlike the broad selection of heterogeneous elements in doping engineering, the introduced and replaced elements are congeneric in alloy engineering. With a general formula of $MX_{2(1-x)}X'_{2x}$ or $M_{1-x}M'_xX_2$, TMD alloys exhibit intriguing properties when the ratios of the components are changed.

Among $MX_{2(1-x)}X'_{2x}$ alloys, $MoS_{2(1-x)}Se_{2x}$ is the representative one and has been widely studied. Ersan *et al.* studied the adsorption and diffusion of Li on $MoS_{2(1-x)}Se_{2x}$ monolayers, where x varied from 0 to 1 (Fig. 9a and b).[189] With the diffusion pathway shown in Fig. 9a, MoS_2 and $MoSe_2$ systems exhibit two symmetrical absolute energy maxima, an absolute energy minimum and a local energy minimum. The diffusion energy barriers of Li on MoS_2 and $MoSe_2$ are 0.194 and 0.237 eV. When x changes from 0.33 to 0.66, due to the introduction of congeneric elements, two asymmetrical energy maxima are observed, including an absolute maximum and a local energy maximum, and there are still one local and one absolute minimum in the case of $x = 0.33$ and 0.66. For $x = 0.5$, two local minima and one absolute minimum are observed. The diffusion energy barriers are 0.319, 0.541, and 0.391 eV for $MoS_{2(1-x)}Se_{2x}$ alloys with x = 0.33, 0.5, and 0.66. From the calculations, it can be observed that Li prefers to bind with S. Although the diffusion energy barriers of these alloys increase, they are not very high values that are still acceptable for assuring moderate Li diffusion kinetics. The penetration barriers were also explored with varying x values (Fig. 9b). The results show that the penetration energy barriers decrease with increasing x from 0 to 1, indicating that the increasing concentration of Se is beneficial for the penetration of Li. However, a barrier energy of 1.283 eV is still large. One of the reasons may be attributed to the increased crystal constant with increasing Se concentration.

Among $M_{1-x}M'_xX_2$, the $Mo_{1-x}W_xS_2$ alloys have received much attention. Barik *et al.* explored monolayer $Mo_{1-x}W_xS_2$ as anode materials for Li storage *via* theoretical calculations (Fig. 9c–j).[190] For pristine monolayer $Mo_{1-x}W_xS_2$, the DOS and

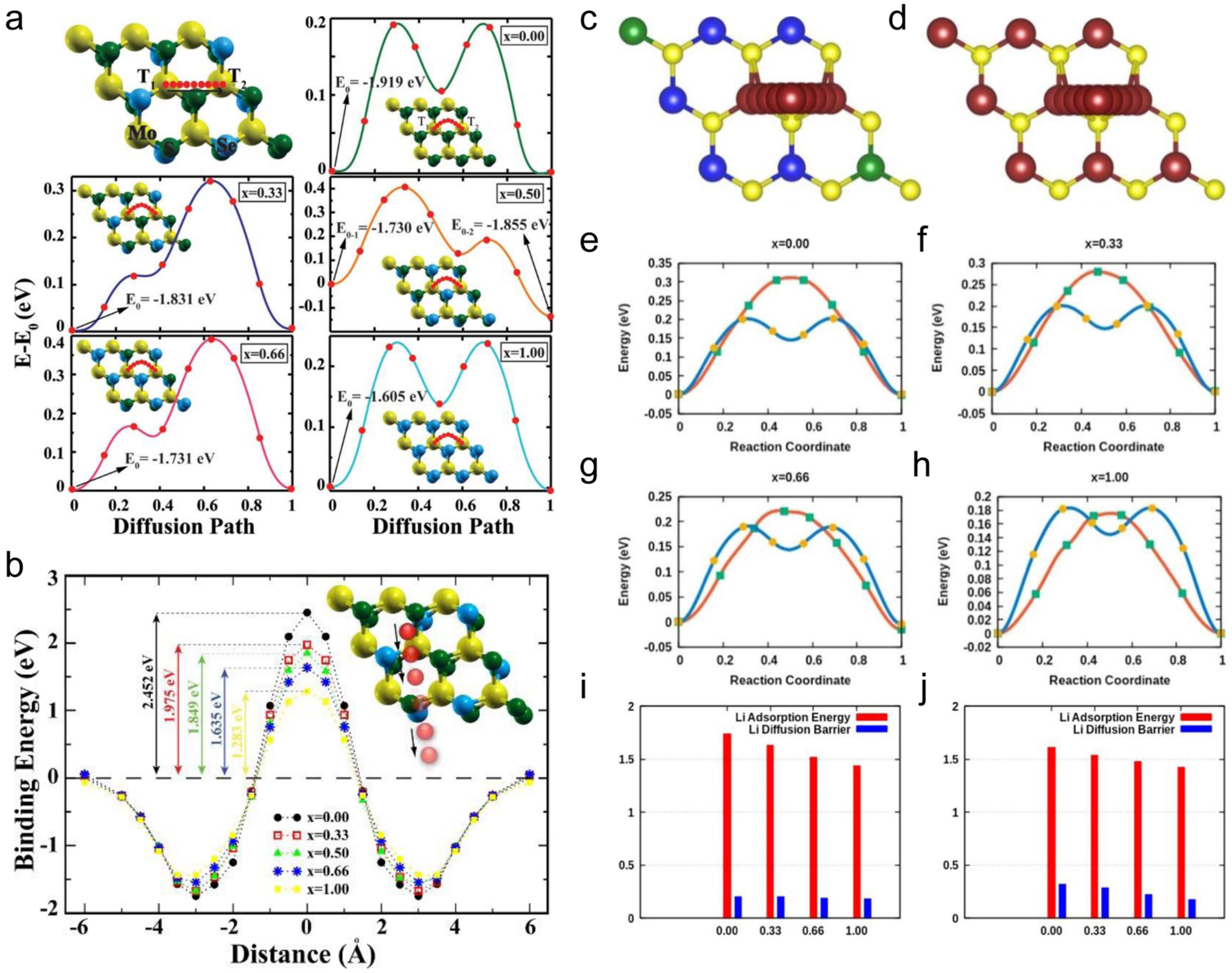

Fig. 9 Diffusion path and binding energies of Li in monolayer TMDs. (a) Lowest energy diffusion paths of a single lithium atom and calculated energy profiles along the paths for one Li atom-adsorbed on the TMD monolayer. (b) Binding energies of a single lithium atom when it approaches and penetrates bare $MoS_{2(1-x)}Se_{2x}$ monolayers from infinity. Schematic representation of the Li diffusion path in the $Mo_{1-x}W_xS_2$ alloy of $x = 0.33$ from one top position to another through the hollow site. (c) Bare surface and (d) lithiated surface. The blue, green, yellow, and maroon balls denote Mo, W, S, and Li atoms, respectively. (e–h) Energy profiles for lithium diffusion on monolayer $Mo_{1-x}W_xS_2$. The blue line indicates a bare surface, and the red line indicates a lithiated surface. Li adsorption energies and diffusion barriers on monolayer $Mo_{1-x}W_xS_2$ compared to different compositions of x. (i) Migration of Li on the bare surface and (j) migration of Li on the lithiated surface. Reproduced with permission from (a and b) ref. 189. Copyright 2015, American Chemical Society; (c–j) ref. 190. Copyright 2018, American Chemical Society.

the band gaps do not change much with different ratios of Mo and W. After lithiation, the conduction band minima of monolayer $Mo_{1-x}W_xS_2$ move towards the Fermi level, suggesting the formation of the metallic phase, which is consistent with the fact that the intercalation of alkali metal ions into Mo and W-based dichalcogenides can induce the formation of the metallic phase.[62,108] With the diffusion pathway shown in Fig. 9c and d, they studied the diffusion energy barriers of Li on pristine and lithiated $Mo_{1-x}W_xS_2$ (Fig. 9e–h).[190] The pristine MoS_2 and WS_2 systems exhibit two symmetrical absolute maxima. However, the two maxima are not symmetrical in the case of alloys. The maximum at the T_{Mo} site is always slightly higher than that at the T_W site, indicating the stronger bonding interaction between Mo and Li. The lithiated $Mo_{1-x}W_xS_2$ systems exhibit similar characteristics to pristine $Mo_{1-x}W_xS_2$ systems except for the disappearance of the local energy minima due to the repulsion between Li atoms. The Li adsorption and its diffusion energy barriers in pristine and lithiated $Mo_{1-x}W_xS_2$ indicate that they all decrease with increasing W ratios (Fig. 9i and j).

Different from the studies performed by Ersan and Barik *et al.*,[189,190] Chaney and coworkers performed a comprehensive study of the adsorption and diffusion of Li on Janus Mo/WXY (X, Y = S, Se, Te), where the ratio of X and Y was fixed at 1 : 1.[191] According to the adsorption energy results of both regular and Janus TMDs (Fig. 10a and b), it can be concluded that the binding interaction between chalcogen and Li follows the order of S > Se > Te, and for Mo and W, the binding interaction follows the order of Mo > W. The diffusion of Li on regular and Janus TMDs indicates that the diffusion barriers of Li on the X side of Janus MXYs are comparable to that on MX_2 (Fig. 10c and d), while the diffusion barriers of Li on the Y side of Janus MXYs are always lower than that on the X side due to the weaker interaction between Li and Y.

According to the calculations, alloying is an effective strategy to balance the adsorption and diffusion of ions on TMDs. This also applies to some other properties for $MX_{2(1-x)}X'_{2x}$ under similar conditions of the same ion storage capacity. The alloys will balance the theoretical specific capacity of TMD electrodes. For example, the relative atomic mass of S is lower than that of Se. Therefore, increasing the content of S in $MSe_{2(1-x)}S_{2x}$ will reduce the relative molecular mass of $MSe_{2(1-x)}S_{2x}$. However, the ion storage capacity of $MSe_{2(1-x)}S_{2x}$ will not change with the variation of the ratios of Se and S due to the same ion storage mechanism in MoS_2 and $MoSe_2$. As a result, the theoretical specific capacity of $MSe_{2(1-x)}S_{2x}$ will increase with increasing the content of S.[192,193] Although increasing the Se content would reduce the theoretical specific capacity of $MSe_{2(1-x)}S_{2x}$, Se has a larger atomic radius than S, which can enlarge the interlayer spacing of $MSe_{2(1-x)}S_{2x}$, resulting in reduced ion diffusion barriers (Fig. 11a and b).[54,194,195] In addition to the increased specific capacity and the enlarged interlayer spacing, the incorporation of S or Se can also induce the structural rearrangement and the electron redistribution of $MSe_{2(1-x)}S_{2x}$, leading to the formation of abundant anion vacancies and the metallic phase, which can increase the active adsorption sites and enhance the conductivity of $MSe_{2(1-x)}S_{2x}$.[56,196–198] He *et al.* fabricated $MoS_{2(1-x)}Se_{2x}$ alloys through partial substitution of S for Se in $MoSe_2$. They found that the alloying process can generate anion vacancies, and the vacancy concentration can be adjusted by tuning the ratios of S and Se.[55] With a S : Se ratio close to 1 : 1, the largest vacancy concentration and the best electrochemical performance are achieved (Fig. 11c–e). Huang *et al.* synthesized MoSSe@rGo for Na^+ storage,[198] and in their Raman spectra, the 1T-$MoSe_2$ and 1T-MoS_2 modes were observed in both MoSSe and MoSSe@rGO, indicating the formation of a metallic phase by the alloying process (Fig. 11f). For $M_{1-x}M'_xX_2$, a similar phenomenon was also observed.[199,200] Besides, there is an additional possibility that introducing the M elements from metallic phase MX_2 into semiconducting phase $M'X_2$ may endow $M_{1-x}M'_xX_2$ with interesting properties. Our group explored this possibility by introducing V into MoS_2 to form $Mo_{1-x}V_xS_2$ for Li storage.[201] The introduction of V into MoS_2 makes $Mo_{1-x}V_xS_2$ exhibit semi-metallic conductivity, making $Mo_{1-x}V_xS_2$ exhibit enhanced conductivity and better electrochemical performance than pristine 2H-MoS_2.

As discussed above, the different elements in $MX_{2(1-x)}X'_{2x}$ or $M_{1-x}M'_xX_2$ alloys have different influences. Therefore, it is important to manipulate the x values to optimize the electrochemical performance of TMD alloys. However, the optimal x values reported by different studies vary. For example, He and Yu *et al.* found that the electrochemical performance of $MoS_{2(1-x)}Se_{2x}$ becomes the best when $x = 0.5$.[55,197] However, Cai and coworkers believed that $x = 0.25$ is the optimal value for the $MoS_{2(1-x)}Se_{2x}$ alloys.[202] For $Mo_{1-x}W_xS_2$, a similar issue also exists.[53,203] The optimal values of x may be due to the other factors that can also affect the electrochemical performance of TMD alloys, such as the morphology and the types of stored ions, which need comprehensive and detailed studies.

In short, alloy engineering is expected to balance different properties of TMDs, such as the metallic phase formation and the interlayer spacing enlargement. Defect introduction can also be achieved by alloying; however, the issue that needs to be clarified is determining the optimal x value and its influencing factors in TMD alloy systems.

3.6 Bond modulation

Different from the several mainstream molecular modulation strategies discussed above, the bond modulation strategy focuses on the impact of chemical bonds on the properties of TMDs, including bond length, bond angle, bond energy, and additionally created chemical bonds.[170,204] For example, by manipulating the bond length, the interlayer spacing can be modulated,[164,205] and the enhanced bond energy can stabilize the intercalation reaction, although it will make it more difficult for the conversion reaction to occur.[168,169] The additional chemical bond formation in TMDs shows more possibilities in comparison and has therefore been studied more extensively. For instance, covalent interactions usually exist between the introduced guests and the transition metals or chalcogens in TMDs so they can be stably bonded at room temperature and modulate the TMDs' properties.[145,154] Our group has demonstrated that the introduced Se atoms between the interlayers of

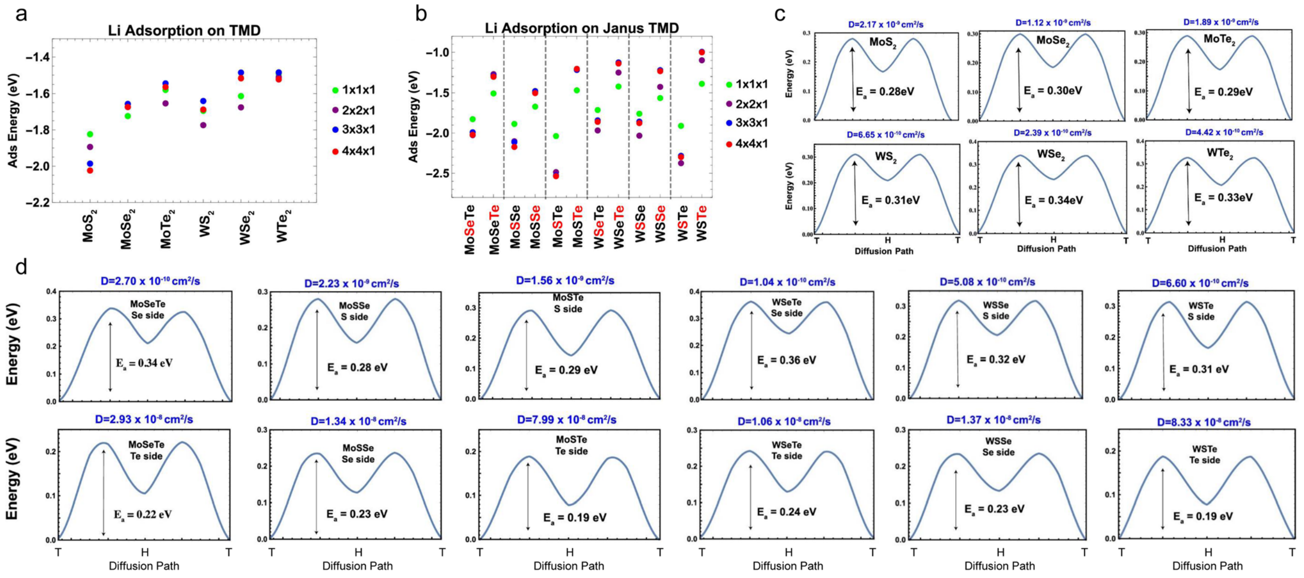

Fig. 10 Adsorption energies for a Li atom over metal-top sites of all supercell sizes. (a) Mo- and W-based TMDs and (b) top and bottom sides of Janus structures. The red color on the chalcogen atom of Janus structures on the *x*-axis labeling indicates the side on which the Li atom is adsorbed. (c) Activation energy barriers for Li atom diffusion for regular TMD-MX_2 (M = Mo, W; X = S, Se, Te), calculated with the nudged elastic band (NEB) method simulations. (d) Activation energy barriers for Li atom diffusion for Janus TMD MXY (M = Mo, W; X/Y = S, Se, Te), calculated with NEB simulations. Reproduced with permission from (a–d) ref. 191. Copyright 2021, American Chemical Society.

$MoSe_2$ form covalent Se–Se bonds with the Se in $MoSe_2$,[58] and the covalent Se–Se bonds not only enlarge the interlayer spacing of $MoSe_2$ but also prevent the Se shuttle effects. The S–Co–S covalent bonds formed by intercalating Co into MoS_2 interlayers can induce the formation of the 1T phase, expand the interlayer spacing of MoS_2, and serve as electrical pathways to accelerate

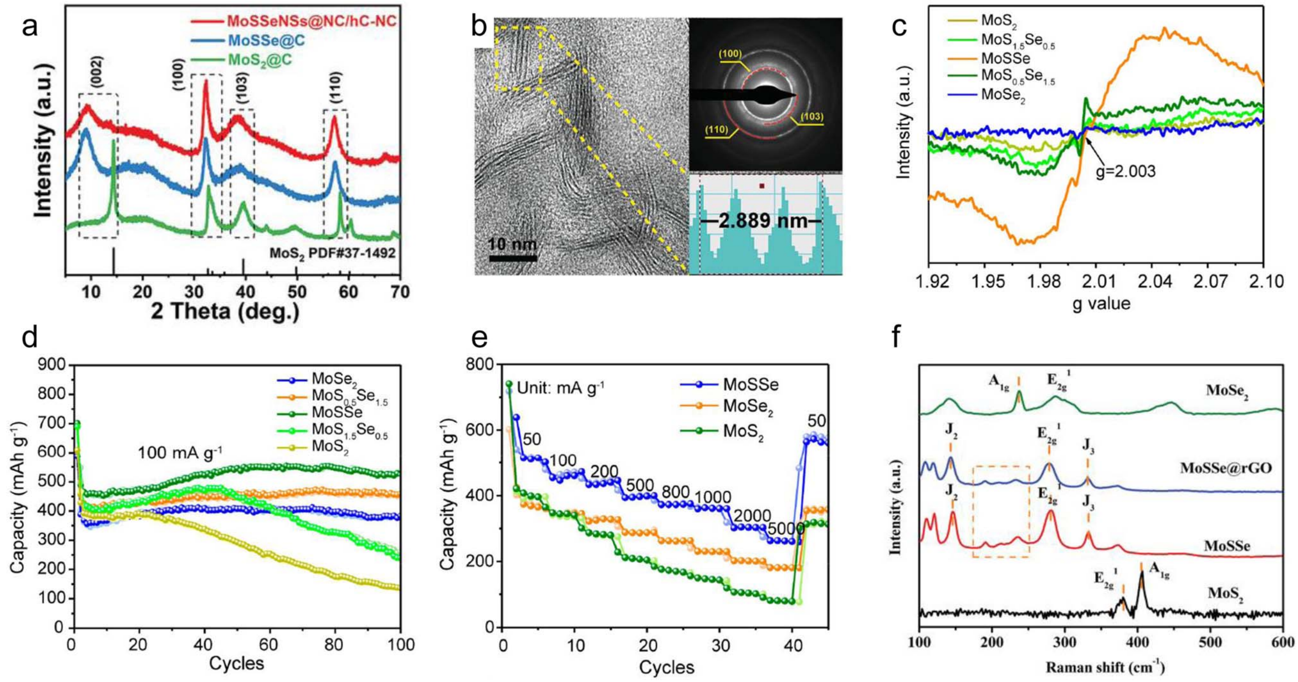

Fig. 11 Structural, electrochemical, and Raman properties of $MoS_{2(1-x)}Se_{2x}$ alloys. (a) XRD patterns of MoSSeNSs@NC/hC-NC, MoSSe@C and MoS_2@C. (b) HRTEM image of MoSSeNSs@NC/hC-NC. (c) EPR results of $MoSe_2$, MoSSe, and MoS_2. (d) Cycling performance at 100 mA g^{-1} for all the as-prepared samples. (e) Rate capability of $MoSe_2$, MoSSe, and MoS_2. (f) Raman spectra of as-prepared MoSSe@rGO, MoSSe, MoS_2, and $MoSe_2$ samples. MoSSeNSs@NC/hC-NC: MoSSe nanosheets supported on hollow cubic N-doped carbon. Reproduced with permission from (a and b) ref. 195. Copyright 2021, Wiley-VCH; (c–e) ref. 55. Copyright 2019, American Chemical Society; (f) ref. 198. Copyright 2020, Wiley-VCH.

interlayer charge transfer, thus greatly improving the electrochemical performance of MoS_2.[141] In addition, introducing additional chemical bonds by incorporating additional atoms into TMDs can also lead to interesting phenomena. For example, Zhang *et al.* prepared unusual red $MoSe_2$ nanosheets by introducing an oxygen gradient on the surface of $MoSe_2$ nanosheets and forming Mo–O bonds.[57] The formation of Mo–O bonds induces the formation of high valence Mo, thereby regulating the band gap of red $MoSe_2$ and enhancing its electrical conductivity. A similar enhanced electrical conductivity was also observed when incorporating P and N atoms into TMDs due to the formation of M–P and M–N bonds.[109,182,206]

In short, the bond modulation strategy modulates the properties of TMDs from a chemical bonding viewpoint. The bond length, bond angle, bond energy, and additional chemical bonding all impact the electrochemical performance of TMDs. However, they have not received widespread attention yet, and some systematic studies are lacking, thus needing further exploration in the future.

4. Summary and perspectives

In summary, this review outlines the basic properties of TMDs and discusses the molecular modulation strategies of TMDs by combining computational and experimental studies towards their application in metal ion batteries. In brief, due to the different coordination and stacking sequences of transition metals, TMDs show polymorphs and stacking polytypes. Among them, 1T and 2H phase TMDs are widely studied in metal ion batteries. The coordination environment of transition metals and the filling states of their d orbitals determine the electrical properties of TMDs. When the orbitals are fully occupied, semiconducting behaviour is exhibited, such as in 2H-MoS_2 and 2H-$MoSe_2$. When the orbitals are partially filled, metallic conductivity is exhibited, such as in 2H-NbS_2 and 1T-VS_2. In addition, the chalcogen atoms can also affect the electronic properties of TMDs, although their influence is not significant. When TMDs are used as alkali metal-ion battery electrodes, reversible intercalation and extraction reactions occur at a relatively high cutoff voltage (~1 V). As the intercalation process continues, the subsequent reaction mechanism depends on the M–X bond strength of TMDs. If the M–X bonding interactions are stronger than the A–MX_2 interactions, reversible intercalation and extraction reactions, such as in TiX_2 and NbX_2, will continue. In contrast, conversion reactions will occur if the M–X bonding interactions are weaker than the A–MX_2 interactions, and the reversibility of the conversion reactions depends on the dynamic properties of TMDs. Excellent dynamic properties of TMDs contribute to reversible conversion reactions, such as in VX_2, while poor dynamic properties of TMDs lead to irreversible conversion reactions, such as in MoX_2, WX_2, and ReX_2. Only intercalation and extraction reactions have been reported when TMD electrodes are used in multivalent-ion batteries.

Several molecular modulation strategies of TMDs, including phase engineering, defect engineering, interlayer spacing expansion, heteroatom doping, alloy engineering, and bond modulation, are also discussed. By combining theoretical and experimental studies, the basic mechanisms of different molecular modulation strategies and their specific effects on the properties of TMDs for storing metal ions are summarized, (1) phase engineering aims at improving the intrinsic electrical conductivity of semiconducting TMDs; (2) defect engineering can provide more active adsorption sites and decrease the length of the ion diffusion pathway; (3) the interlayer spacing expansion strategy is beneficial for reducing the diffusion energy barriers for metal ions in TMDs; (4) heteroatom doping

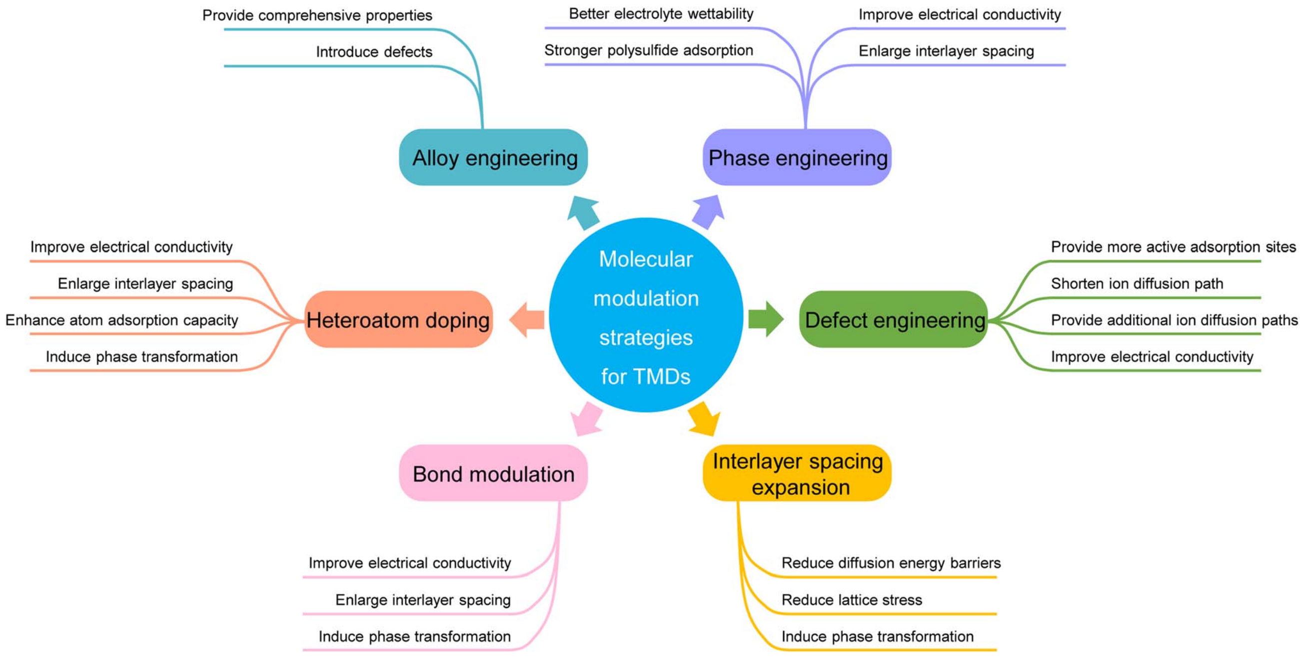

Fig. 12 A schematic summarizing the influences of different molecular modulation strategies on the properties of TMDs.

is expected to improve the electrical conductivity and the atom adsorption capacity of TMDs; (5) alloy engineering is used to obtain comprehensive properties of TMDs; (6) bond modulation can enhance the electrical conductivity and the ion diffusion dynamics of TMDs. In addition to the main effects mentioned above, some extra advantages of molecular modulation strategies toward specific applications are also summarized (Fig. 12).

Although many advances have been achieved in developing TMD electrodes, much effort is still needed to further promote the development of TMDs as electrode materials from a molecular modulation viewpoint. (1) The conversion reaction provides high discharge capacity for some TMD electrodes, while the reversibility of the conversion reaction is not satisfactory. Although it has been reported that the dynamic properties of TMDs influence the reversibility of the conversion reaction, VX_2 compounds with excellent dynamic properties only exhibit a partially reversible conversion reaction. Therefore, extensive theoretical and experimental research on the dynamic properties of the conversion reaction at the molecular and atomic level is needed to make it fully reversible, which is crucial for employing TMDs in metal-ion batteries. (2) The precise modulation methods for TMD molecules are necessary to be developed, which only exist in the theoretical models currently. By manipulating TMD molecules precisely, the specific mechanisms and effects of various molecular modulation strategies can be better understood. In addition, the properties of TMDs can be flexibly adjusted to meet different needs, which is beneficial for providing more potential opportunities and leveraging the maximum advantages of TMDs. (3) Deeper theoretical calculations need to be performed to help understand the reaction mechanisms of TMDs and direct the experimental designs. Currently, most theoretical calculations focus on the level of single-layer or double-layer TMDs, which is very different from the actual situation. Therefore, many conclusions drawn from calculations are inconsistent with the experimental data, and the real mechanisms cannot be verified. (4) In the future, various *in situ* characterization techniques which can reveal the basic reaction mechanisms of TMDs before and after molecular modulation need to be developed. Despite significant progress in research on TMDs in recent years, there are still a large number of problems which need to be solved. By developing advanced *in situ* characterization techniques, many problems can be understood and solved from the source, which is helpful for developing practice and high-performance TMD electrodes with balanced and optimized properties.

Author contributions

B. L. and J. Z. designed the scope of the paper. M. G. surveyed the relevant literature, and all authors wrote the paper.

Conflicts of interest

There are no conflicts to declare.

Acknowledgements

B. L. acknowledges financial support from the National Natural Science Foundation of China no. U20A20247 and 51922038. M. G. acknowledges financial support from the Postgraduate Scientific Research Innovation Project of Hunan Province no. CX20230407. A. M. R. acknowledges financial support through Clemson University's R. A. Bowen Fellowship funds.

References

1 M. Armand and J. M. Tarascon, Building better batteries, *Nature*, 2008, **451**, 652–657.
2 Z. Zhu, T. Jiang, M. Ali, Y. Meng, Y. Jin, Y. Cui and W. Chen, Rechargeable Batteries for Grid Scale Energy Storage, *Chem. Rev.*, 2022, **122**, 16610–16751.
3 K. Chen, X. Shen, L. Luo, H. Chen, R. Cao, X. Feng, W. Chen, Y. Fang and Y. Cao, Correlating the Solvating Power of Solvents with the Strength of Ion-Dipole Interaction in Electrolytes of Lithium-ion Batteries, *Angew. Chem., Int. Ed.*, 2023, **62**, e202312373.
4 Y. Li, F. Wu, Y. Li, M. Liu, X. Feng, Y. Bai and C. Wu, Ether-based electrolytes for sodium ion batteries, *Chem. Soc. Rev.*, 2022, **51**, 4484–4536.
5 R. Usiskin, Y. Lu, J. Popovic, M. Law, P. Balaya, Y.-S. Hu and J. Maier, Fundamentals, status and promise of sodium-based batteries, *Nat. Rev. Mater.*, 2021, **6**, 1020–1035.
6 K. Chayambuka, G. Mulder, D. L. Danilov and P. H. L. Notten, From Li-Ion Batteries toward Na-Ion Chemistries: Challenges and Opportunities, *Adv. Energy Mater.*, 2020, **10**, 2001310.
7 Y. Feng, Y. Lv, H. Fu, M. Parekh, A. M. Rao, H. Wang, X. Tai, X. Yi, Y. Lin, J. Zhou and B. Lu, Co-activation for enhanced K-ion storage in battery anodes, *Natl. Sci. Rev.*, 2023, **10**, nwad118.
8 M. Gu, A. M. Rao, J. Zhou and B. Lu, In situ formed uniform and elastic SEI for high-performance batteries, *Energy Environ. Sci.*, 2023, **16**, 1166–1175.
9 H. Ding, J. Wang, J. Zhou, C. Wang and B. Lu, Building electrode skins for ultra-stable potassium metal batteries, *Nat. Commun.*, 2023, **14**, 2305.
10 Y. Liu, Y. Shi, C. Gao, Z. Shi, H. Ding, Y. Feng, Y. He, J. Sha, J. Zhou and B. Lu, Low-Temperature Potassium Batteries Enabled by Electric and Thermal Field Regulation, *Angew. Chem., Int. Ed.*, 2023, **62**, e202300016.
11 G. Fang, J. Zhou, A. Pan and S. Liang, Recent Advances in Aqueous Zinc-Ion Batteries, *ACS Energy Lett.*, 2018, **3**, 2480–2501.
12 C. Liu, X. Xie, B. Lu, J. Zhou and S. Liang, Electrolyte Strategies toward Better Zinc-Ion Batteries, *ACS Energy Lett.*, 2021, **6**, 1015–1033.
13 N. Zhang, X. Chen, M. Yu, Z. Niu, F. Cheng and J. Chen, Materials chemistry for rechargeable zinc-ion batteries, *Chem. Soc. Rev.*, 2020, **49**, 4203–4219.
14 B. Chen, D. Chao, E. Liu, M. Jaroniec, N. Zhao and S.-Z. Qiao, Transition metal dichalcogenides for alkali

metal ion batteries: engineering strategies at the atomic level, *Energy Environ. Sci.*, 2020, **13**, 1096–1131.

15 H. Shuai, R. Liu, W. Li, X. Yang, H. Lu, Y. Gao, J. Xu and K. Huang, Recent Advances of Transition Metal Sulfides/Selenides Cathodes for Aqueous Zinc-Ion Batteries, *Adv. Energy Mater.*, 2023, **13**, 2202992.

16 L. Wang, Q. Zhang, J. Zhu, X. Duan, Z. Xu, Y. Liu, H. Yang and B. Lu, Nature of extra capacity in MoS_2 electrodes: molybdenum atoms accommodate with lithium, *Energy Storage Mater.*, 2019, **16**, 37–45.

17 M. S. Whittingham, Electrical Energy Storage and Intercalation Chemistry, *Science*, 1976, **192**, 1126–1127.

18 T. Wang, S. Chen, H. Pang, H. Xue and Y. Yu, MoS_2-Based Nanocomposites for Electrochemical Energy Storage, *Adv. Sci.*, 2017, **4**, 1600289.

19 X. Ren, Q. Zhao, W. D. McCulloch and Y. Wu, MoS_2 as a long-life host material for potassium ion intercalation, *Nano Res.*, 2017, **10**, 1313–1321.

20 W. S. V. Lee, T. Xiong, X. Wang and J. Xue, Unraveling MoS_2 and Transition Metal Dichalcogenides as Functional Zinc-Ion Battery Cathode: A Perspective, *Small Methods*, 2021, **5**, 2000815.

21 Y. Li, M. Wang and J. Sun, Molecular Engineering Strategies toward Molybdenum Diselenide Design for Energy Storage and Conversion, *Adv. Energy Mater.*, 2022, **12**, 2202600.

22 Q. Yun, L. Li, Z. Hu, Q. Lu, B. Chen and H. Zhang, Layered Transition Metal Dichalcogenide-Based Nanomaterials for Electrochemical Energy Storage, *Adv. Mater.*, 2020, **32**, 1903826.

23 L. Zhang, H. B. Wu, Y. Yan, X. Wang and X. W. Lou, Hierarchical MoS_2 microboxes constructed by nanosheets with enhanced electrochemical properties for lithium storage and water splitting, *Energy Environ. Sci.*, 2014, **7**, 3302–3306.

24 Y. Wang, W. Kang, X. Pu, Y. Liang, B. Xu, X. Lu, D. Sun and Y. Cao, Template-directed synthesis of $Co_2P/MoSe_2$ in a N-doped carbon hollow structure for efficient and stable sodium/potassium ion storage, *Nano Energy*, 2022, **93**, 106897.

25 B. Jia, Q. Yu, Y. Zhao, M. Qin, W. Wang, Z. Liu, C.-Y. Lao, Y. Liu, H. Wu, Z. Zhang and X. Qu, Bamboo-Like Hollow Tubes with MoS_2/N-Doped-C Interfaces Boost Potassium-Ion Storage, *Adv. Funct. Mater.*, 2018, **28**, 1803409.

26 S. Wang, Y. Si, P. Wan, S. Zhu, W. Chu and Z. Yu, $MoSe_2$ nanoflowers grown on 3D carbon network as an advanced anode for lithium ion batteries, *Mater. Lett.*, 2022, **310**, 131487.

27 M. Hong, J. Li, W. Zhang, S. Liu and H. Chang, Semimetallic 1T′ WTe_2 Nanorods as Anode Material for the Sodium Ion Battery, *Energy Fuels*, 2018, **32**, 6371–6377.

28 J. Ge, L. Fan, J. Wang, Q. Zhang, Z. Liu, E. Zhang, Q. Liu, X. Yu and B. Lu, $MoSe_2$/N-Doped Carbon as Anodes for Potassium-Ion Batteries, *Adv. Energy Mater.*, 2018, **8**, 1801477.

29 D. Sun, D. Ye, P. Liu, Y. Tang, J. Guo, L. Wang and H. Wang, MoS_2/Graphene Nanosheets from Commercial Bulky MoS_2 and Graphite as Anode Materials for High Rate Sodium-Ion Batteries, *Adv. Energy Mater.*, 2018, **8**, 1702383.

30 S. H. Choi, Y. N. Ko, J.-K. Lee and Y. C. Kang, 3D MoS_2–Graphene Microspheres Consisting of Multiple Nanospheres with Superior Sodium Ion Storage Properties, *Adv. Funct. Mater.*, 2015, **25**, 1780–1788.

31 J. Bai, B. Zhao, J. Zhou, J. Si, Z. Fang, K. Li, H. Ma, J. Dai, X. Zhu and Y. Sun, Glucose-Induced Synthesis of 1T-MoS_2/C Hybrid for High-Rate Lithium-Ion Batteries, *Small*, 2019, **15**, 1805420.

32 Y. Zhou, Y. Liu, M. Zhang, Q. Han, Y. Wang, X. Sun, X. Zhang, C. Dong, J. Sun, Z. Tang and F. Jiang, Rationally designed hierarchical N, P co-doped carbon connected 1T/2H-MoS_2 heterostructures with cooperative effect as ultrafast and durable anode materials for efficient sodium storage, *Chem. Eng. J.*, 2022, **433**, 133778.

33 W. Ding, L. Hu, J. Dai, X. Tang, R. Wei, Z. Sheng, C. Liang, D. Shao, W. Song, Q. Liu, M. Chen, X. Zhu, S. Chou, X. Zhu, Q. Chen, Y. Sun and S. X. Dou, Highly Ambient-Stable 1T-MoS_2 and 1T-WS_2 by Hydrothermal Synthesis under High Magnetic Fields, *ACS Nano*, 2019, **13**, 1694–1702.

34 D. Sun, D. Huang, H. Wang, G.-L. Xu, X. Zhang, R. Zhang, Y. Tang, D. Abd Ei-Hady, W. Alshitari, A. Saad Al-Bogami, K. Amine and M. Shao, 1T MoS_2 nanosheets with extraordinary sodium storage properties via thermal-driven ion intercalation assisted exfoliation of bulky MoS_2, *Nano Energy*, 2019, **61**, 361–369.

35 H. He, X. Li, D. Huang, J. Luan, S. Liu, W. K. Pang, D. Sun, Y. Tang, W. Zhou, L. He, C. Zhang, H. Wang and Z. Guo, Electron-Injection-Engineering Induced Phase Transition toward Stabilized 1T-MoS_2 with Extraordinary Sodium Storage Performance, *ACS Nano*, 2021, **15**, 8896–8906.

36 Y. Li, X. Dong, Z. Xu, M. Wang, R. Wang, J. Xie, Y. Ding, P. Su, C. Jiang, X. Zhang, L. Wei, J.-F. Li, Z. Chu, J. Sun and C. Huang, Piezoelectric 1T Phase $MoSe_2$ Nanoflowers and Crystallographically Textured Electrodes for Enhanced Low-Temperature Zinc-Ion Storage, *Adv. Mater.*, 2023, **35**, 2208615.

37 H. Fan, P. Mao, G. Lan, C. Liu, J. Chen, Z. Wang, Z. Li, R. Zheng, Y. Liu and H. Sun, Ultrathin Metallic-Phase Molybdenum Disulfide Nanosheets Stabilized on Functionalized Carbon Nanotubes Via Covalent Interface Interaction for Sodium- and Lithium-Ion Storage, *ACS Appl. Energy Mater.*, 2021, **4**, 9440–9449.

38 B. Chen, H. Lu, N. Zhao, C. Shi, E. Liu, C. He and L. Ma, Facile synthesis and electrochemical properties of continuous porous spheres assembled from defect-rich, interlayer-expanded, and few-layered MoS_2/C nanosheets for reversible lithium storage, *J. Power Sources*, 2018, **387**, 16–23.

39 Z. Lei, J. Zheng, X. He, Y. Wang, X. Yang, F. Xiao, H. Xue, P. Xiong, M. Wei, Q. Chen, Q. Qian and L. Zeng, Defect-rich WS_2–SPAN nanofibers for sodium/potassium-ion batteries: ultralong lifespans and wide-temperature workability, *Inorg. Chem. Front.*, 2023, **10**, 1187–1196.

40 K. Yao, Z. Xu, J. Huang, M. Ma, L. Fu, X. Shen, J. Li and M. Fu, Bundled Defect-Rich MoS_2 for a High-Rate and

Long-Life Sodium-Ion Battery: Achieving 3D Diffusion of Sodium Ion by Vacancies to Improve Kinetics, *Small*, 2019, **15**, 1805405.

41 J. Liang, Z. Wei, C. Wang and J. Ma, Vacancy-induced sodium-ion storage in N-doped carbon Nanofiber@MoS_2 nanosheet arrays, *Electrochim. Acta*, 2018, **285**, 301–308.

42 D. Sha, Y. You, R. Hu, X. Cao, Y. Wei, H. Zhang, L. Pan and Z. Sun, Comprehensively Understanding the Role of Anion Vacancies on K-Ion Storage: A Case Study of Se-Vacancy-Engineered VSe_2, *Adv. Mater.*, 2023, **35**, 2211311.

43 Q. Zhu, W. Li, J. Wu, N. Tian, Y. Li, J. Yang, B. Liu and J. Jiang, Vacancy engineering in WS_2 nanosheets for enhanced potassium-ion storage, *J. Power Sources*, 2022, **542**, 231791.

44 W. Xu, C. Sun, K. Zhao, X. Cheng, S. Rawal, Y. Xu and Y. Wang, Defect engineering activating (boosting) zinc storage capacity of MoS_2, *Energy Storage Mater.*, 2019, **16**, 527–534.

45 Y. Bai, H. Zhang, B. Xiang, X. Liang, J. Hao, C. Zhu and L. Yan, Selenium Defect Boosted Electrochemical Performance of Binder-Free VSe_2 Nanosheets for Aqueous Zinc-Ion Batteries, *ACS Appl. Mater. Interfaces*, 2021, **13**, 23230–23238.

46 H. Wang, H. Jiang, Y. Hu, N. Li, X. Zhao and C. Li, 2D MoS_2/polyaniline heterostructures with enlarged interlayer spacing for superior lithium and sodium storage, *J. Mater. Chem. A*, 2017, **5**, 5383–5389.

47 L. Xing, K. Han, Q. Liu, Z. Liu, J. Chu, L. Zhang, X. Ma, Y. Bao, P. Li and W. Wang, Hierarchical two-atom-layered WSe_2/C ultrathin crumpled nanosheets assemblies: engineering the interlayer spacing boosts potassium-ion storage, *Energy Storage Mater.*, 2021, **36**, 309–317.

48 S. Di, P. Ding, Y. Wang, Y. Wu, J. Deng, L. Jia and Y. Li, Interlayer-expanded MoS_2 assemblies for enhanced electrochemical storage of potassium ions, *Nano Res.*, 2020, **13**, 225–230.

49 M. Huang, Y. Mai, L. Zhao, X. Liang, Z. Fang and X. Jie, Tuning the kinetics of zinc ion in MoS_2 by polyaniline intercalation, *Electrochim. Acta*, 2021, **388**, 138624.

50 Y.-R. Liu, Z.-W. Lei, R.-P. Liu, X.-Y. Li, P.-X. Xiong, Y.-J. Luo, Q.-H. Chen, M.-D. Wei, L.-X. Zeng and Q.-R. Qian, Sn-doped induced stable 1T-WSe_2 nanosheets entrenched on N-doped carbon with extraordinary half/full sodium/potassium storage performance, *Rare Met.*, 2023, **42**, 1557–1569.

51 Y. Zhang, H. Tao, T. Li, S. Du, J. Li, Y. Zhang and X. Yang, Vertically Oxygen-Incorporated MoS_2 Nanosheets Coated on Carbon Fibers for Sodium-Ion Batteries, *ACS Appl. Mater. Interfaces*, 2018, **10**, 35206–35215.

52 S. Li, Y. Liu, X. Zhao, K. Cui, Q. Shen, P. Li, X. Qu and L. Jiao, Molecular Engineering on MoS_2 Enables Large Interlayers and Unlocked Basal Planes for High-Performance Aqueous Zn-Ion Storage, *Angew. Chem., Int. Ed.*, 2021, **60**, 20286–20293.

53 J. Li, H. Yan, W. Wei and L. Meng, Microwave-assisted mass synthesis of $Mo_{1-x}W_xS_2$ alloy composites with a tunable lithium storage property, *Dalton Trans.*, 2018, **47**, 15148–15154.

54 H.-N. Fan, X.-Y. Wang, H.-B. Yu, Q.-F. Gu, S.-L. Chen, Z. Liu, X.-H. Chen, W.-B. Luo and H.-K. Liu, Enhanced Potassium Ion Battery by Inducing Interlayer Anionic Ligands in $MoS_{1.5}Se_{0.5}$ Nanosheets with Exploration of the Mechanism, *Adv. Energy Mater.*, 2020, **10**, 1904162.

55 H. He, D. Huang, Q. Gan, J. Hao, S. Liu, Z. Wu, W. K. Pang, B. Johannessen, Y. Tang, J.-L. Luo, H. Wang and Z. Guo, Anion Vacancies Regulating Endows MoSSe with Fast and Stable Potassium Ion Storage, *ACS Nano*, 2019, **13**, 11843–11852.

56 H. Li, B. Chen, R. Gao, F. Xu, X. Wen, X. Zhong, C. Li, Z. Piao, N. Hu, X. Xiao, F. Shao, G. Zhou and J. Yang, Integrating molybdenum sulfide selenide-based cathode with C-O-Mo heterointerface design and atomic engineering for superior aqueous Zn-ion batteries, *Nano Res.*, 2023, **16**, 4933–4940.

57 S. Zhang, G. Wang, J. Jin, L. Zhang, Z. Wen and J. Yang, Robust and Conductive Red $MoSe_2$ for Stable and Fast Lithium Storage, *ACS Nano*, 2018, **12**, 4010–4018.

58 T. Lei, M. Gu, H. Fu, J. Wang, L. Wang, J. Zhou, H. Liu and B. Lu, Bond modulation of $MoSe_{2+x}$ driving combined intercalation and conversion reactions for high-performance K cathodes, *Chem. Sci.*, 2023, **14**, 2528–2536.

59 M. Chhowalla, H. S. Shin, G. Eda, L.-J. Li, K. P. Loh and H. Zhang, The chemistry of two-dimensional layered transition metal dichalcogenide nanosheets, *Nat. Chem.*, 2013, **5**, 263–275.

60 X. Qian, J. Liu, L. Fu and J. Li, Quantum spin Hall effect in two-dimensional transition metal dichalcogenides, *Science*, 2014, **346**, 1344–1347.

61 Q. H. Wang, K. Kalantar-Zadeh, A. Kis, J. N. Coleman and M. S. Strano, Electronics and optoelectronics of two-dimensional transition metal dichalcogenides, *Nat. Nanotechnol.*, 2012, **7**, 699–712.

62 D. Voiry, A. Mohite and M. Chhowalla, Phase engineering of transition metal dichalcogenides, *Chem. Soc. Rev.*, 2015, **44**, 2702–2712.

63 I. Song, C. Park and H. C. Choi, Synthesis and properties of molybdenum disulphide: from bulk to atomic layers, *RSC Adv.*, 2015, **5**, 7495–7514.

64 S. Jayabal, J. Wu, J. Chen, D. Geng and X. Meng, Metallic 1T-MoS_2 nanosheets and their composite materials: Preparation, properties and emerging applications, *Mater. Today Energy*, 2018, **10**, 264–279.

65 J. Strachan, A. F. Masters and T. Maschmeyer, 3R-MoS_2 in Review: History, Status, and Outlook, *ACS Appl. Energy Mater.*, 2021, **4**, 7405–7418.

66 A. Kumar and P. K. Ahluwalia, A first principle Comparative study of electronic and optical properties of 1H – MoS_2 and 2H – MoS_2, *Mater. Chem. Phys.*, 2012, **135**, 755–761.

67 Y. S. Huang, Preparation, Electrical and Modulation Optical Properties of 2H-MoSe2, *Chin. J. Phys.*, 1984, **22**, 43–53.

68 S. Zhao, T. Hotta, T. Koretsune, K. Watanabe, T. Taniguchi, K. Sugawara, T. Takahashi, H. Shinohara and R. Kitaura, Two-dimensional metallic NbS_2: growth, optical

identification and transport properties, *2D Mater.*, 2016, **3**, 025027.

69 J. Feng, X. Sun, C. Wu, L. Peng, C. Lin, S. Hu, J. Yang and Y. Xie, Metallic Few-Layered VS_2 Ultrathin Nanosheets: High Two-Dimensional Conductivity for In-Plane Supercapacitors, *J. Am. Chem. Soc.*, 2011, **133**, 17832–17838.

70 W. Choi, N. Choudhary, G. H. Han, J. Park, D. Akinwande and Y. H. Lee, Recent development of two-dimensional transition metal dichalcogenides and their applications, *Mater. Today*, 2017, **20**, 116–130.

71 J. Li, B. Zhao, P. Chen, R. Wu, B. Li, Q. Xia, G. Guo, J. Luo, K. Zang, Z. Zhang, H. Ma, G. Sun, X. Duan and X. Duan, Synthesis of Ultrathin Metallic MTe_2 (M = V, Nb, Ta) Single-Crystalline Nanoplates, *Adv. Mater.*, 2018, **30**, 1801043.

72 H. Liu, Y. Xue, J.-A. Shi, R. A. Guzman, P. Zhang, Z. Zhou, Y. He, C. Bian, L. Wu, R. Ma, J. Chen, J. Yan, H. Yang, C.-M. Shen, W. Zhou, L. Bao and H.-J. Gao, Observation of the Kondo Effect in Multilayer Single-Crystalline VTe_2 Nanoplates, *Nano Lett.*, 2019, **19**, 8572–8580.

73 C. Zhu, D. Gao, J. Ding, D. Chao and J. Wang, TMD-based highly efficient electrocatalysts developed by combined computational and experimental approaches, *Chem. Soc. Rev.*, 2018, **47**, 4332–4356.

74 E. Torun, H. Sahin, S. Cahangirov, A. Rubio and F. M. Peeters, Anisotropic electronic, mechanical, and optical properties of monolayer WTe_2, *J. Appl. Phys.*, 2016, **119**, 074307.

75 M. Rahman, K. Davey and S.-Z. Qiao, Advent of 2D Rhenium Disulfide (ReS_2): Fundamentals to Applications, *Adv. Funct. Mater.*, 2017, **27**, 1606129.

76 H.-X. Zhong, S. Gao, J.-J. Shi and L. Yang, Quasiparticle band gaps, excitonic effects, and anisotropic optical properties of the monolayer distorted 1T diamond-chain structures ReS_2 and $ReSe_2$, *Phys. Rev. B: Condens. Matter Mater. Phys.*, 2015, **92**, 115438.

77 J. A. Wilson and A. D. Yoffe, The transition metal dichalcogenides discussion and interpretation of the observed optical, electrical and structural properties, *Adv. Phys.*, 1969, **18**, 193–335.

78 L. Peng, Y. Zhu, D. Chen, R. S. Ruoff and G. Yu, Two-Dimensional Materials for Beyond-Lithium-Ion Batteries, *Adv. Energy Mater.*, 2016, **6**, 1600025.

79 S. Hao, X. Shen, M. Tian, R. Yu, Z. Wang and L. Chen, Reversible conversion of MoS_2 upon sodium extraction, *Nano Energy*, 2017, **41**, 217–224.

80 X. Fang, C. Hua, X. Guo, Y. Hu, Z. Wang, X. Gao, F. Wu, J. Wang and L. Chen, Lithium storage in commercial MoS_2 in different potential ranges, *Electrochim. Acta*, 2012, **81**, 155–160.

81 T. Zhao, H. Shu, Z. Shen, H. Hu, J. Wang and X. Chen, Electrochemical Lithiation Mechanism of Two-Dimensional Transition-Metal Dichalcogenide Anode Materials: Intercalation versus Conversion Reactions, *J. Phys. Chem. C*, 2019, **123**, 2139–2146.

82 L. Zhang, D. Sun, J. Kang, J. Feng, H. A. Bechtel, L.-W. Wang, E. J. Cairns and J. Guo, Electrochemical Reaction Mechanism of the MoS_2 Electrode in a Lithium-Ion Cell Revealed by in Situ and Operando X-ray Absorption Spectroscopy, *Nano Lett.*, 2018, **18**, 1466–1475.

83 J. Zhou, L. Wang, M. Yang, J. Wu, F. Chen, W. Huang, N. Han, H. Ye, F. Zhao, Y. Li and Y. Li, Hierarchical VS_2 Nanosheet Assemblies: A Universal Host Material for the Reversible Storage of Alkali Metal Ions, *Adv. Mater.*, 2017, **29**, 1702061.

84 L. Zhang, D. Sun, Q. Wei, H. Ju, J. Feng, J. Zhu, L. Mai, E. J. Cairns and J. Guo, Understanding the electrochemical reaction mechanism of VS_2 nanosheets in lithium-ion cells by multiple in situ and ex situ x-ray spectroscopy, *J. Phys. D: Appl. Phys.*, 2018, **51**, 494001.

85 C. Yang, J. Feng, F. Lv, J. Zhou, C. Lin, K. Wang, Y. Zhang, Y. Yang, W. Wang, J. Li and S. Guo, Metallic Graphene-Like VSe_2 Ultrathin Nanosheets: Superior Potassium-Ion Storage and Their Working Mechanism, *Adv. Mater.*, 2018, **30**, 1800036.

86 G. Wang, Y. Zhang, H. S. Cho, X. Zhao, F. Kim and J. Zou, Revisiting the Structural Evolution of MoS_2 During Alkali Metal (Li, Na, and K) Intercalation, *ACS Appl. Energy Mater.*, 2021, **4**, 14180–14190.

87 V. P. H. Huy, Y. N. Ahn and J. Hur, Recent Advances in Transition Metal Dichalcogenide Cathode Materials for Aqueous Rechargeable Multivalent Metal-Ion Batteries, *Nanomaterials*, 2021, **11**, 1517.

88 K. Yao, Z. Xu, M. Ma, J. Li, F. Lu and J. Huang, Densified Metallic MoS_2/Graphene Enabling Fast Potassium-Ion Storage with Superior Gravimetric and Volumetric Capacities, *Adv. Funct. Mater.*, 2020, **30**, 2001484.

89 S. Yan, W. Qiao, X. He, X. Guo, L. Xi, W. Zhong and Y. Du, Enhancement of magnetism by structural phase transition in MoS_2, *Appl. Phys. Lett.*, 2015, **106**, 012408.

90 T. Xiang, S. Tao, W. Xu, Q. Fang, C. Wu, D. Liu, Y. Zhou, A. Khalil, Z. Muhammad, W. Chu, Z. Wang, H. Xiang, Q. Liu and L. Song, Stable 1T-$MoSe_2$ and Carbon Nanotube Hybridized Flexible Film: Binder-Free and High-Performance Li-Ion Anode, *ACS Nano*, 2017, **11**, 6483–6491.

91 K. Wu, X. Cao, M. Li, B. Lei, J. Zhan and M. Wu, Bottom-Up Synthesis of MoS_2/CNTs Hollow Polyhedron with 1T/2H Hybrid Phase for Superior Potassium-Ion Storage, *Small*, 2020, **16**, 2004178.

92 M. Srinivaas, C.-Y. Wu, J.-G. Duh and J. M. Wu, Highly Rich 1T Metallic Phase of Few-Layered WS_2 Nanoflowers for Enhanced Storage of Lithium-Ion Batteries, *ACS Sustain. Chem. Eng.*, 2019, **7**, 10363–10370.

93 M. Acerce, D. Voiry and M. Chhowalla, Metallic 1T phase MoS_2 nanosheets as supercapacitor electrode materials, *Nat. Nanotechnol.*, 2015, **10**, 313–318.

94 L. Liu, W. Yang, H. Chen, X. Chen, K. Zhang, Q. Zeng, S. Lei, J. Huang, S. Li and S. Peng, High zinc-ion intercalation reaction activity of MoS_2 cathode based on regulation of thermodynamic metastability and interlayer water, *Electrochim. Acta*, 2022, **410**, 140016.

95 Y. Liu and X. Wu, Recent Advances of Transition Metal Chalcogenides as Cathode Materials for Aqueous Zinc-Ion Batteries, *Nanomaterials*, 2022, **12**, 3298.

96 J. He, G. Hartmann, M. Lee, G. S. Hwang, Y. Chen and A. Manthiram, Freestanding 1T MoS_2/graphene heterostructures as a highly efficient electrocatalyst for lithium polysulfides in Li–S batteries, *Energy Environ. Sci.*, 2019, **12**, 344–350.

97 J. Liu, N. Gong, W. Peng, Y. Li, F. Zhang and X. Fan, Vertically aligned 1 T phase MoS_2 nanosheet array for high-performance rechargeable aqueous Zn-ion batteries, *Chem. Eng. J.*, 2022, **428**, 130981.

98 J. Liu, P. Xu, J. Liang, H. Liu, W. Peng, Y. Li, F. Zhang and X. Fan, Boosting aqueous zinc-ion storage in MoS_2 via controllable phase, *Chem. Eng. J.*, 2020, **389**, 124405.

99 W.-H. Ryu, J.-W. Jung, K. Park, S.-J. Kim and I.-D. Kim, Vine-like MoS_2 anode materials self-assembled from 1-D nanofibers for high capacity sodium rechargeable batteries, *Nanoscale*, 2014, **6**, 10975–10981.

100 B. Yu, Y. Chen, Z. Wang, D. Chen, X. Wang, W. Zhang, J. He and W. He, 1T-MoS_2 nanotubes wrapped with N-doped graphene as highly-efficient absorbent and electrocatalyst for Li–S batteries, *J. Power Sources*, 2020, **447**, 227364.

101 M. Wang, L. Fan, D. Tian, X. Wu, Y. Qiu, C. Zhao, B. Guan, Y. Wang, N. Zhang and K. Sun, Rational Design of Hierarchical SnO_2/1T-MoS_2 Nanoarray Electrode for Ultralong-Life Li–S Batteries, *ACS Energy Lett.*, 2018, **3**, 1627–1633.

102 H. Shu, F. Li, C. Hu, P. Liang, D. Cao and X. Chen, The capacity fading mechanism and improvement of cycling stability in MoS_2-based anode materials for lithium-ion batteries, *Nanoscale*, 2016, **8**, 2918–2926.

103 Y. Zhang, Z. Mu, C. Yang, Z. Xu, S. Zhang, X. Zhang, Y. Li, J. Lai, Z. Sun, Y. Yang, Y. Chao, C. Li, X. Ge, W. Yang and S. Guo, Rational Design of MXene/1T-2H MoS_2-C Nanohybrids for High-Performance Lithium–Sulfur Batteries, *Adv. Funct. Mater.*, 2018, **28**, 1707578.

104 Z. Lei, J. Zhan, L. Tang, Y. Zhang and Y. Wang, Recent Development of Metallic (1T) Phase of Molybdenum Disulfide for Energy Conversion and Storage, *Adv. Energy Mater.*, 2018, **8**, 1703482.

105 W.-j. Tang, X.-l. Wang, D. Xie, X.-h. Xia, C.-d. Gu and J.-p. Tu, Hollow metallic 1T MoS_2 arrays grown on carbon cloth: a freestanding electrode for sodium ion batteries, *J. Mater. Chem. A*, 2018, **6**, 18318–18324.

106 J. Wu, J. Liu, J. Cui, S. Yao, M. Ihsan-Ul-Haq, N. Mubarak, E. Quattrocchi, F. Ciucci and J.-K. Kim, Dual-phase MoS_2 as a high-performance sodium-ion battery anode, *J. Mater. Chem. A*, 2020, **8**, 2114–2122.

107 Z. Zhao, T. Xu and X. Yu, Unlock the Potassium Storage Behavior of Single-Phased Tungsten Selenide Nanorods via Large Cation Insertion, *Adv. Mater.*, 2023, **35**, 2208096.

108 F. Liu, Y. Zou, X. Tang, L. Mao, D. Du, H. Wang, M. Zhang, Z. Wang, N. Yao, W. Zhao, M. Bai, T. Zhao, Y. Liu and Y. Ma, Phase Engineering and Alkali Cation Stabilization for 1T Molybdenum Dichalcogenides Monolayers, *Adv. Funct. Mater.*, 2022, **32**, 2204601.

109 H. He, H. Zhang, D. Huang, W. Kuang, X. Li, J. Hao, Z. Guo and C. Zhang, Harnessing Plasma-Assisted Doping Engineering to Stabilize Metallic Phase MoSe2 for Fast and Durable Sodium-Ion Storage, *Adv. Mater.*, 2022, **34**, 2200397.

110 P. Li, Y. Yang, S. Gong, F. Lv, W. Wang, Y. Li, M. Luo, Y. Xing, Q. Wang and S. Guo, Co-doped 1T-MoS_2 nanosheets embedded in N, S-doped carbon nanobowls for high-rate and ultra-stable sodium-ion batteries, *Nano Res.*, 2019, **12**, 2218–2223.

111 P. Xiong, R. Ma, N. Sakai, L. Nurdiwijayanto and T. Sasaki, Unilamellar Metallic MoS_2/Graphene Superlattice for Efficient Sodium Storage and Hydrogen Evolution, *ACS Energy Lett.*, 2018, **3**, 997–1005.

112 Y. Fang, Y. Lv, F. Gong, A. A. Elzatahry, G. Zheng and D. Zhao, Synthesis of 2D-Mesoporous-Carbon/MoS_2 Heterostructures with Well-Defined Interfaces for High-Performance Lithium-Ion Batteries, *Adv. Mater.*, 2016, **28**, 9385–9390.

113 M. Jiang, Y. Hu, B. Mao, Y. Wang, Z. Yang, T. Meng, X. Wang and M. Cao, Strain-regulated Gibbs free energy enables reversible redox chemistry of chalcogenides for sodium ion batteries, *Nat. Commun.*, 2022, **13**, 5588.

114 X. Chia, A. Y. S. Eng, A. Ambrosi, S. M. Tan and M. Pumera, Electrochemistry of Nanostructured Layered Transition-Metal Dichalcogenides, *Chem. Rev.*, 2015, **115**, 11941–11966.

115 R. Zhou, H. Wang, J. Chang, C. Yu, H. Dai, Q. Chen, J. Zhou, H. Yu, G. Sun and W. Huang, Ammonium Intercalation Induced Expanded 1T-Rich Molybdenum Diselenides for Improved Lithium Ion Storage, *ACS Appl. Mater. Interfaces*, 2021, **13**, 17459–17466.

116 J. Yang, J. Wang, L. Zhu, X. Wang, X. Dong, W. Zeng, J. Wang and F. Pan, Boosting magnesium storage in MoS_2 via a 1T phase introduction and interlayer expansion strategy: theoretical prediction and experimental verification, *Sustain. Energy Fuels*, 2021, **5**, 5471–5480.

117 W. Zong, C. Yang, L. Mo, Y. Ouyang, H. Guo, L. Ge, Y.-E. Miao, D. Rao, J. Zhang, F. Lai and T. Liu, Elucidating dual-defect mechanism in rhenium disulfide nanosheets with multi-dimensional ion transport channels for ultrafast sodium storage, *Nano Energy*, 2020, **77**, 105189.

118 J. Mei, Y. Zhang, T. Liao, Z. Sun and S. X. Dou, Strategies for improving the lithium-storage performance of 2D nanomaterials, *Natl. Sci. Rev.*, 2018, **5**, 389–416.

119 Y. Zhao, D. Yang, T. He, J. Li, L. Wei, D. Wang, Y. Wang, X. Wang, G. Chen and Y. Wei, Vacancy engineering in VS_2 nanosheets for ultrafast pseudocapacitive sodium ion storage, *Chem. Eng. J.*, 2021, **421**, 129715.

120 T. Liu, N. Peng, X. Zhang, R. Zheng, M. Xia, H. Yu, M. Shui, Y. Xie and J. Shu, Controllable defect engineering enhanced bond strength for stable electrochemical energy storage, *Nano Energy*, 2021, **79**, 105460.

121 F. Liu and Z. Fan, Defect engineering of two-dimensional materials for advanced energy conversion and storage, *Chem. Soc. Rev.*, 2023, **52**, 1723–1772.

122 Y. Jia, K. Jiang, H. Wang and X. Yao, The Role of Defect Sites in Nanomaterials for Electrocatalytic Energy Conversion, *Chem*, 2019, **5**, 1371–1397.

123 P. Gao, Z. Chen, Y. Gong, R. Zhang, H. Liu, P. Tang, X. Chen, S. Passerini and J. Liu, The Role of Cation Vacancies in Electrode Materials for Enhanced Electrochemical Energy Storage: Synthesis, Advanced Characterization, and Fundamentals, *Adv. Energy Mater.*, 2020, **10**, 1903780.

124 G. Barik and S. Pal, Defect Induced Performance Enhancement of Monolayer MoS_2 for Li- and Na-Ion Batteries, *J. Phys. Chem. C*, 2019, **123**, 21852–21865.

125 J. Kunstmann, T. B. Wendumu and G. Seifert, Localized defect states in MoS_2 monolayers: electronic and optical properties, *Phys. Status Solidi B*, 2017, **254**, 1600645.

126 Y. Li, R. Zhang, W. Zhou, X. Wu, H. Zhang and J. Zhang, Hierarchical MoS_2 Hollow Architectures with Abundant Mo Vacancies for Efficient Sodium Storage, *ACS Nano*, 2019, **13**, 5533–5540.

127 T. Liu, X. Zhang, M. Xia, H. Yu, N. Peng, C. Jiang, M. Shui, Y. Xie, T.-F. Yi and J. Shu, Functional cation defects engineering in TiS_2 for high-stability anode, *Nano Energy*, 2020, **67**, 104295.

128 J. Zhang, A. Yang, X. Wu, J. van de Groep, P. Tang, S. Li, B. Liu, F. Shi, J. Wan, Q. Li, Y. Sun, Z. Lu, X. Zheng, G. Zhou, C.-L. Wu, S.-C. Zhang, M. L. Brongersma, J. Li and Y. Cui, Reversible and selective ion intercalation through the top surface of few-layer MoS_2, *Nat. Commun.*, 2018, **9**, 5289.

129 Y. Liu, B. V. Merinov and W. A. Goddard, Origin of low sodium capacity in graphite and generally weak substrate binding of Na and Mg among alkali and alkaline earth metals, *Proc. Natl. Acad. Sci. U. S. A.*, 2016, **113**, 3735–3739.

130 F. Zhu, H. Zhang, Z. Lu, D. Kang and L. Han, Controlled defective engineering of MoS_2 nanosheets for rechargeable Mg batteries, *J. Energy Storage*, 2021, **42**, 103046.

131 Q. Zhang, S. Tan, R. G. Mendes, Z. Sun, Y. Chen, X. Kong, Y. Xue, M. H. Rümmeli, X. Wu, S. Chen and L. Fu, Extremely Weak van der Waals Coupling in Vertical ReS_2 Nanowalls for High-Current-Density Lithium-Ion Batteries, *Adv. Mater.*, 2016, **28**, 2616–2623.

132 S. Tongay, H. Sahin, C. Ko, A. Luce, W. Fan, K. Liu, J. Zhou, Y.-S. Huang, C.-H. Ho, J. Yan, D. F. Ogletree, S. Aloni, J. Ji, S. Li, J. Li, F. M. Peeters and J. Wu, Monolayer behaviour in bulk ReS_2 due to electronic and vibrational decoupling, *Nat. Commun.*, 2014, **5**, 3252.

133 J. Xu, J. Zhang, W. Zhang and C.-S. Lee, Interlayer Nanoarchitectonics of Two-Dimensional Transition-Metal Dichalcogenides Nanosheets for Energy Storage and Conversion Applications, *Adv. Energy Mater.*, 2017, **7**, 1700571.

134 L. Wu, M. Gu, Y. Feng, S. Chen, L. Fan, X. Yu, K. Guo, J. Zhou and B. Lu, Layered Superconductor $Cu_{0.11}TiSe_2$ as a High-Stable K-Cathode, *Adv. Funct. Mater.*, 2022, **32**, 2109893.

135 J. Shuai, H. D. Yoo, Y. Liang, Y. Li, Y. Yao and L. C. Grabow, Density functional theory study of Li, Na, and Mg intercalation and diffusion in MoS_2 with controlled interlayer spacing, *Mater. Res. Express*, 2016, **3**, 064001.

136 N. Zheng, G. Jiang, X. Chen, J. Mao, Y. Zhou and Y. Li, Rational design of a tubular, interlayer expanded MoS_2–N/O doped carbon composite for excellent potassium-ion storage, *J. Mater. Chem. A*, 2019, **7**, 9305–9315.

137 Y. Li, D. Wu, Z. Zhou, C. R. Cabrera and Z. Chen, Enhanced Li Adsorption and Diffusion on MoS_2 Zigzag Nanoribbons by Edge Effects: A Computational Study, *J. Phys. Chem. Lett.*, 2012, **3**, 2221–2227.

138 H. J. Chen, J. Huang, X. L. Lei, M. S. Wu, G. Liu, C. Y. Ouyang and B. Xu, Adsorption and Diffusion of Lithium on MoS_2 Monolayer: The Role of Strain and Concentration, *Int. J. Electrochem. Sci.*, 2013, **8**, 2196–2203.

139 H. Hwang, H. Kim and J. Cho, MoS_2 Nanoplates Consisting of Disordered Graphene-like Layers for High Rate Lithium Battery Anode Materials, *Nano Lett.*, 2011, **11**, 4826–4830.

140 H. Liu, D. Su, R. Zhou, B. Sun, G. Wang and S. Z. Qiao, Highly Ordered Mesoporous MoS_2 with Expanded Spacing of the (002) Crystal Plane for Ultrafast Lithium Ion Storage, *Adv. Energy Mater.*, 2012, **2**, 970–975.

141 K. Ma, Y. Liu, H. Jiang, Y. Hu, R. Si, H. Liu and C. Li, Multivalence-Ion Intercalation Enables Ultrahigh 1T Phase MoS_2 Nanoflowers to Enhanced Sodium-Storage Performance, *CCS Chem.*, 2020, **3**, 1472–1482.

142 G. Du, Z. Guo, S. Wang, R. Zeng, Z. Chen and H. Liu, Superior stability and high capacity of restacked molybdenum disulfide as anode material for lithium ion batteries, *Chem. Commun.*, 2010, **46**, 1106–1108.

143 E. Benavente, M. A. S. Ana, F. Mendizábal and G. González, Intercalation chemistry of molybdenum disulfide, *Coord. Chem. Rev.*, 2002, **224**, 87–109.

144 K. D. Rasamani, F. Alimohammadi and Y. Sun, Interlayer-expanded MoS_2, *Mater. Today*, 2017, **20**, 83–91.

145 W. M. R. Divigalpitiya, R. F. Frindt and S. R. Morrison, Inclusion Systems of Organic Molecules in Restacked Single-Layer Molybdenum Disulfide, *Science*, 1989, **246**, 369–371.

146 A. Zak, Y. Feldman, V. Lyakhovitskaya, G. Leitus, R. Popovitz-Biro, E. Wachtel, H. Cohen, S. Reich and R. Tenne, Alkali Metal Intercalated Fullerene-Like MS_2 ($M = W$, Mo) Nanoparticles and Their Properties, *J. Am. Chem. Soc.*, 2002, **124**, 4747–4758.

147 Z. Hu, L. Wang, K. Zhang, J. Wang, F. Cheng, Z. Tao and J. Chen, MoS_2 Nanoflowers with Expanded Interlayers as High-Performance Anodes for Sodium-Ion Batteries, *Angew. Chem., Int. Ed.*, 2014, **53**, 12794–12798.

148 G. González, M. A. S. Ana, E. Benavente, J. P. Donoso, T. J. Bonagamba, N. C. Mello and H. Panepucci, Electrical conductivity and lithium diffusion in molybdenum disulfide intercalated with poly(ethylene oxide), *Solid State Ionics*, 1996, **85**, 225–230.

149 W. Ye, F. Wu, N. Shi, H. Zhou, Q. Chi, W. Chen, S. Du, P. Gao, H. Li and S. Xiong, Metal–Semiconductor Phase Twinned Hierarchical MoS_2 Nanowires with Expanded

Interlayers for Sodium-Ion Batteries with Ultralong Cycle Life, *Small*, 2020, **16**, 1906607.

150 R. Bissessur and P. K. Y. Liu, Direct insertion of polypyrrole into molybdenum disulfide, *Solid State Ionics*, 2006, **177**, 191–196.

151 Y. Li, Y. Liang, F. C. R. Hernandez, H. D. Yoo, Q. An and Y. Yao, Enhancing sodium-ion battery performance with interlayer-expanded MoS_2–PEO nanocomposites, *Nano Energy*, 2015, **15**, 453–461.

152 K. Chang, W. Chen, L. Ma, H. Li, H. Li, F. Huang, Z. Xu, Q. Zhang and J.-Y. Lee, Graphene-like MoS_2/amorphous carbon composites with high capacity and excellent stability as anode materials for lithium ion batteries, *J. Mater. Chem.*, 2011, **21**, 6251–6257.

153 Y. Liu, X. Wang, X. Song, Y. Dong, L. Yang, L. Wang, D. Jia, Z. Zhao and J. Qiu, Interlayer expanded MoS_2 enabled by edge effect of graphene nanoribbons for high performance lithium and sodium ion batteries, *Carbon*, 2016, **109**, 461–471.

154 Y. Liu, Y. Yuan, L. Peng, L. Cheng, B. An, Y. Wang, Q. Wei, X. Xia and H. Zhou, Study on the construction of interlayer adjustable C@MoS_2 fiber anode by biomass confining and its lithium/sodium storage mechanism, *ChemSusChem*, 2023, e202300576.

155 H. Jiang, D. Ren, H. Wang, Y. Hu, S. Guo, H. Yuan, P. Hu, L. Zhang and C. Li, 2D Monolayer MoS_2–Carbon Interoverlapped Superstructure: Engineering Ideal Atomic Interface for Lithium Ion Storage, *Adv. Mater.*, 2015, **27**, 3687–3695.

156 N. Feng, R. Meng, L. Zu, Y. Feng, C. Peng, J. Huang, G. Liu, B. Chen and J. Yang, A polymer-direct-intercalation strategy for MoS_2/carbon-derived heteroaerogels with ultrahigh pseudocapacitance, *Nat. Commun.*, 2019, **10**, 1372.

157 H. Liang, Z. Cao, F. Ming, W. Zhang, D. H. Anjum, Y. Cui, L. Cavallo and H. N. Alshareef, Aqueous Zinc-Ion Storage in MoS_2 by Tuning the Intercalation Energy, *Nano Lett.*, 2019, **19**, 3199–3206.

158 P. Jing, H. Lu, W. Yang and Y. Cao, Interlayer-expanded and binder-free VS_2 nanosheets assemblies for enhanced Mg^{2+} and Li^+/Mg^{2+} hybrid ion storage, *Electrochim. Acta*, 2020, **330**, 135263.

159 M. Wang, H. Ye, V. Vasudevan and N. V. Medhekar, Enhancing kinetic and electrochemical performance of layered MoS_2 cathodes with interlayer expansion for Mg-ion batteries, *J. Power Sources*, 2022, **542**, 231722.

160 S. Li, Y. Liu, X. Zhao, Q. Shen, W. Zhao, Q. Tan, N. Zhang, P. Li, L. Jiao and X. Qu, Sandwich-Like Heterostructures of MoS_2/Graphene with Enlarged Interlayer Spacing and Enhanced Hydrophilicity as High-Performance Cathodes for Aqueous Zinc-Ion Batteries, *Adv. Mater.*, 2021, **33**, 2007480.

161 Y. Liang, H. D. Yoo, Y. Li, J. Shuai, H. A. Calderon, F. C. R. Hernandez, L. C. Grabow and Y. Yao, Interlayer-Expanded Molybdenum Disulfide Nanocomposites for Electrochemical Magnesium Storage, *Nano Lett.*, 2015, **15**, 2194–2202.

162 H. D. Yoo, Y. Liang, H. Dong, J. Lin, H. Wang, Y. Liu, L. Ma, T. Wu, Y. Li, Q. Ru, Y. Jing, Q. An, W. Zhou, J. Guo, J. Lu, S. T. Pantelides, X. Qian and Y. Yao, Fast kinetics of magnesium monochloride cations in interlayer-expanded titanium disulfide for magnesium rechargeable batteries, *Nat. Commun.*, 2017, **8**, 339.

163 F. Cui, M. Han, W. Zhou, C. Lai, Y. Chen, J. Su, J. Wang, H. Li and Y. Hu, Superlattice-Stabilized WSe_2 Cathode for Rechargeable Aluminum Batteries, *Small Methods*, 2022, **6**, 2201281.

164 Q. Liu, X. Weijun, Z. Wu, J. Huo, D. Liu, Q. Wang and S. Wang, The origin of the enhanced performance of nitrogen-doped MoS_2 in lithium ion batteries, *Nanotechnology*, 2016, **27**, 175402.

165 Y. Cai, H. Yang, J. Zhou, Z. Luo, G. Fang, S. Liu, A. Pan and S. Liang, Nitrogen doped hollow MoS_2/C nanospheres as anode for long-life sodium-ion batteries, *Chem. Eng. J.*, 2017, **327**, 522–529.

166 A. A. Kotsun, V. A. Alekseev, S. G. Stolyarova, A. A. Makarova, M. A. Grebenkina, A. P. Zubareva, A. V. Okotrub and L. G. Bulusheva, Effect of molybdenum disulfide doping with substitutional nitrogen and sulfur vacancies on lithium intercalation, *J. Alloys Compd.*, 2023, **947**, 169689.

167 Y.-C. Lin, D. O. Dumcenco, H.-P. Komsa, Y. Niimi, A. V. Krasheninnikov, Y.-S. Huang and K. Suenaga, Properties of Individual Dopant Atoms in Single-Layer MoS_2: Atomic Structure, Migration, and Enhanced Reactivity, *Adv. Mater.*, 2014, **26**, 2857–2861.

168 H. Shan, J. Qin, J. Wang, H. M. K. Sari, L. Lei, W. Xiao, W. Li, C. Xie, H. Yang, Y. Luo, G. Zhang and X. Li, Doping-Induced Electronic/Ionic Engineering to Optimize the Redox Kinetics for Potassium Storage: A Case Study of Ni-Doped $CoSe_2$, *Adv. Sci.*, 2022, **9**, 2200341.

169 P. Wen, H. Wang, X. Wang, H. Wang, Y. Bai and Z. Yang, Exploring the physicochemical role of Pd dopant in promoting Li-ion diffusion dynamics and storage performance of NbS_2 at the atomic scale, *Phys. Chem. Chem. Phys.*, 2022, **24**, 14877–14885.

170 S. Sovizi and R. Szoszkiewicz, Single atom doping in 2D layered MoS_2 from a periodic table perspective, *Surf. Sci. Rep.*, 2022, **77**, 100567.

171 X.-L. Fan, Y.-R. An and W.-J. Guo, Ferromagnetism in Transitional Metal-Doped MoS_2 Monolayer, *Nanoscale Res. Lett.*, 2016, **11**, 154.

172 Y. C. Cheng, Z. Y. Zhu, W. B. Mi, Z. B. Guo and U. Schwingenschlögl, Prediction of two-dimensional diluted magnetic semiconductors: Doped monolayer MoS_2 systems, *Phys. Rev. B: Condens. Matter Mater. Phys.*, 2013, **87**, 100401.

173 Q. Ding, W. Zheng, A. Zhao, Y. Zhao, K. Chen, X. Zhou, H. Zhang, Q. Li, X. Ai, H. Yang, Y. Fang and Y. Cao, W-Doping Induced Efficient Tunnel-to-Layered Structure Transformation of $Na_{0.44}Mn_{1-x}W_xO_2$: Phase Evolution, Sodium-Storage Properties, and Moisture Stability, *Adv. Energy Mater.*, 2023, **13**, 2203802.

174 L. Xiao, F. Ji, J. Zhang, X. Chen and Y. Fang, Doping Regulation in Polyanionic Compounds for Advanced Sodium-Ion Batteries, *Small*, 2023, **19**, 2205732.

175 X. Zhao, P. Chen, C. Xia, T. Wang and X. Dai, Electronic and magnetic properties of n-type and p-doped MoS_2 monolayers, *RSC Adv.*, 2016, **6**, 16772–16778.

176 S. Lu, C. Li, Y. F. Zhao, Y. Y. Gong, L. Y. Niu and X. J. Liu, Tunable redox potential of nonmetal doped monolayer MoS_2: first principle calculations, *Appl. Surf. Sci.*, 2016, **384**, 360–367.

177 X. Sun and Z. Wang, Adsorption and diffusion of lithium on heteroatom-doped monolayer molybdenum disulfide, *Appl. Surf. Sci.*, 2018, **455**, 911–918.

178 R. Tian, A. Wu, G. Zhang, J. Liu, R. A. P. Camacho, W. Yu, S. Zhou, M. Yao and H. Huang, Adsorption and diffusion of alkali metals (Li, Na, and K) on heteroatom-doped monolayer titanium disulfide, *Dalton Trans.*, 2021, **50**, 7065–7077.

179 D. Wang, Y. Liu, X. Meng, Y. Wei, Y. Zhao, Q. Pang and G. Chen, Two-dimensional VS_2 monolayers as potential anode materials for lithium-ion batteries and beyond: first-principles calculations, *J. Mater. Chem. A*, 2017, **5**, 21370–21377.

180 F. Li, Y. Qu and M. Zhao, Germanium sulfide nanosheet: a universal anode material for alkali metal ion batteries, *J. Mater. Chem. A*, 2016, **4**, 8905–8912.

181 H. R. Jiang, W. Shyy, M. Liu, L. Wei, M. C. Wu and T. S. Zhao, Boron phosphide monolayer as a potential anode material for alkali metal-based batteries, *J. Mater. Chem. A*, 2017, **5**, 672–679.

182 S. Qin, W. Lei, D. Liu and Y. Chen, Advanced N-doped mesoporous molybdenum disulfide nanosheets and the enhanced lithium-ion storage performance, *J. Mater. Chem. A*, 2016, **4**, 1440–1445.

183 H. Xie, B. Chen, C. Liu, G. Wu, S. Sui, E.-Z. Liu, G. Zhou, C. He, W. Hu and N. Q. Zhao, Engineering the Interfacial Doping of 2D Heterostructures with Good Bidirectional Reaction Kinetics for Durably Reversible Sodium-Ion Batteries, *Energy Storage Mater.*, 2023, **60**, 102830.

184 J. Zhao, D. Xiao, Q. Wan, X. Wei, G. Tao, Y. Liu, Y. Xiang, K. Davey, Z. Liu, Z. Guo and Y. Song, Molybdenum Atom Engineered Vanadium Disulfide for Boosted High-Capacity Li-Ion Storage, *Small*, 2023, 2301738.

185 P. Wang, Z. Shen, Y. Xia, H. Wang, L. Zheng, W. Xi and S. Zhan, Atomic Insights for Optimum and Excess Doping in Photocatalysis: A Case Study of Few-Layer Cu-$ZnIn_2S_4$, *Adv. Funct. Mater.*, 2019, **29**, 1807013.

186 J. Zhang, C. Du, Z. Dai, W. Chen, Y. Zheng, B. Li, Y. Zong, X. Wang, J. Zhu and Q. Yan, NbS_2 Nanosheets with M/Se (M = Fe, Co, Ni) Codopants for Li^+ and Na^+ Storage, *ACS Nano*, 2017, **11**, 10599–10607.

187 T. Wang, C. Sun, M. Yang, G. Zhao, S. Wang, F. Ma, L. Zhang, Y. Shao, Y. Wu, B. Huang and X. Hao, Phase-transformation engineering in MoS_2 on carbon cloth as flexible binder-free anode for enhancing lithium storage, *J. Alloys Compd.*, 2017, **716**, 112–118.

188 Z. Sheng, P. Qi, Y. Lu, G. Liu, M. Chen, X. Gan, Y. Qin, K. Hao and Y. Tang, Nitrogen-Doped Metallic MoS_2 Derived from a Metal–Organic Framework for Aqueous Rechargeable Zinc-Ion Batteries, *ACS Appl. Mater. Interfaces*, 2021, **13**, 34495–34506.

189 F. Ersan, G. Gökoğlu and E. Aktürk, Adsorption and Diffusion of Lithium on Monolayer Transition Metal Dichalcogenides ($MoS_{2(1-x)}Se_{2x}$) Alloys, *J. Phys. Chem. C*, 2015, **119**, 28648–28653.

190 G. Barik and S. Pal, Monolayer Transition-Metal Dichalcogenide $Mo_{1-x}W_xS_2$ Alloys as Efficient Anode Materials for Lithium-Ion Batteries, *J. Phys. Chem. C*, 2018, **122**, 25837–25848.

191 G. Chaney, A. Ibrahim, F. Ersan, D. Çakır and C. Ataca, Comprehensive Study of Lithium Adsorption and Diffusion on Janus Mo/WXY (X, Y = S, Se, Te) Using First-Principles and Machine Learning Approaches, *ACS Appl. Mater. Interfaces*, 2021, **13**, 36388–36406.

192 J. Shi, H. Li, Y. Liu, Q. Lu and F. Gao, Molybdenum Sulfide Selenide Nanosheets Synergized with Nitrogen-Rich Carbon Frameworks toward High Performance and Stable Sodium Storage, *Adv. Mater. Interfaces*, 2022, **9**, 2102408.

193 Y. Yang, S. Wang, J. Zhang, H. Li, Z. Tang and X. Wang, Nanosheet-assembled $MoSe_2$ and S-doped $MoSe_{2-x}$ nanostructures for superior lithium storage properties and hydrogen evolution reactions, *Inorg. Chem. Front.*, 2015, **2**, 931–937.

194 G. Jia, D. Chao, N. H. Tiep, Z. Zhang and H. J. Fan, Intercalation Na-ion storage in two-dimensional $MoS_{2-x}Se_x$ and capacity enhancement by selenium substitution, *Energy Storage Mater.*, 2018, **14**, 136–142.

195 B. Liu, Y. Liu, X. Hu, G. Zhong, J. Li, J. Yuan and Z. Wen, N-Doped Carbon Modifying MoSSe Nanosheets on Hollow Cubic Carbon for High-Performance Anodes of Sodium-Based Dual-Ion Batteries, *Adv. Funct. Mater.*, 2021, **31**, 2101066.

196 K. Zhang, H. Zhang, C. Li and X. Ma, Vertically oriented $MoSe_{0.4}S_{1.6}$/N-doped C nanostructures directly grown on carbon nanotubes as high-performance anode for potassium-ion batteries, *J. Electroanal. Chem.*, 2022, **923**, 116846.

197 X. Yu, G. Zhao, C. Wu, H. Huang, C. Liu, X. Shen, M. Wang, X. Bai and N. Zhang, Constructing anion vacancy-rich MoSSe/G van der Waals heterostructures for high-performance Mg–Li hybrid-ion batteries, *J. Mater. Chem. A*, 2021, **9**, 23276–23285.

198 Y. Huang, Z. Wang, M. Guan, F. Wu and R. Chen, Toward Rapid-Charging Sodium-Ion Batteries using Hybrid-Phase Molybdenum Sulfide Selenide-Based Anodes, *Adv. Mater.*, 2020, 32, 2003534.

199 A. Kutana, E. S. Penev and B. I. Yakobson, Engineering electronic properties of layered transition-metal dichalcogenide compounds through alloying, *Nanoscale*, 2014, **6**, 5820–5825.

200 C. Tan, W. Zhao, A. Chaturvedi, Z. Fei, Z. Zeng, J. Chen, Y. Huang, P. Ercius, Z. Luo, X. Qi, B. Chen, Z. Lai, B. Li, X. Zhang, J. Yang, Y. Zong, C. Jin, H. Zheng, C. Kloc and

H. Zhang, Preparation of Single-Layer $MoS_{2x}Se_{2(1-x)}$ and $Mo_xW_{1-x}S_2$ Nanosheets with High-Concentration Metallic 1T Phase, *Small*, 2016, **12**, 1866–1874.

201 Q. Zhang, L. Wang, J. Wang, X. Yu, J. Ge, H. Zhang and B. Lu, Semimetallic vanadium molybdenum sulfide for high-performance battery electrodes, *J. Mater. Chem. A*, 2018, **6**, 9411–9419.

202 G. Cai, L. Peng, S. Ye, Y. Huang, G. Wang and X. Zhang, Defect-rich $MoS_{2(1-x)}Se_{2x}$ few-layer nanocomposites: a superior anode material for high-performance lithium-ion batteries, *J. Mater. Chem. A*, 2019, **7**, 9837–9843.

203 J. Xu, L. Dong, H. Tang and C. Li, Facile synthesis of $Mo_{0.91}W_{0.09}S_2$ ultrathin nanosheets/amorphous carbon composites for lithium-ion battery anode, *Ceram. Int.*, 2016, **42**, 7803–7809.

204 J. Dong, Y. Zhao, G. Ouyang and G. Yang, A perspective on optimizing photoelectric conversion process in 2D transition-metal dichalcogenides and related heterostructures, *Appl. Phys. Lett.*, 2022, **120**, 080501.

205 P. Tao, J. He, T. Shen, Y. Hao, J. Yan, Z. Huang, X. Xu, M. Li and Y. Chen, Nitrogen-Doped MoS_2 Foam for Fast Sodium Ion Storage, *Adv. Mater. Interfaces*, 2019, **6**, 1900460.

206 T. Wang, C. Sun, M. Yang, L. Zhang, Y. Shao, Y. Wu and X. Hao, Enhanced reversible lithium ion storage in stable 1T@2H WS_2 nanosheet arrays anchored on carbon fiber, *Electrochim. Acta*, 2018, **259**, 1–8.